A THESIS

FOR THE DEGREE OF DOCTOR OF PHILOSOPHY

Enhancing Microwave Absorption for Measurement Sensitivity Improvement in Thermoelastic Optical Indicator Microscopy Through Metamaterial Integration

SHEWANGZAW HAMELO

Department of physics

GRADUATE SCHOOL

JEJU NATIONAL UNIVERSITY

December 2023

Enhancing Microwave Absorption for Measurement Sensitivity Improvement in Thermoelastic Optical Indicator Microscopy Through Metamaterial Integration

A dissertation submitted in partial FULFILLMENT of the requirements
for the degree of Doctor of Philosophy [Physics]

Shewangzaw Hamelo

Jeju National University Graduate School

Department of physics

Supervised by Professor Han Ju Lee

A Dissertation has been approved by the dissertation committee.

2023.12

Chair	Jungkial Kim
Member	Younghan
Member	Hanju Lee
Member	Myung-Hwa Jung

Abstract

This study is devoted to improving the measurement sensitivity of thermoelastic optical indicator microscopy (TEOIM) by enhancing microwave absorption within the optical indicator (OI). OI, the fundamental component of TEOIM, consists of a glass substrate coated with a thin film, and the sensitivity of TEOIM is closely related to the efficiency of microwave absorption within the OI.

In this work, two approaches were implemented to study microwave absorption enhancement based on the OI. First, the microwave absorption of OI with different film thicknesses was investigated. For this purpose, aluminum-coated glass with film thicknesses of 10nm, 25nm, 50nm, 75 nm, and 100nm was fabricated. Their corresponding microwave absorption was investigated by measuring the microwave near-field. The results show a clear correlation between the thickness of the thin films of OI and the absorption of the microwave near field. 10nm showed an increased absorption of microwaves. This correlation indicates that the reduction of thin film thickness of the OI has a higher sensitivity to the microwave near field.

Second, the microwave absorption of OI is investigated by integrating it with the metamaterial absorber. The metamaterial absorber resonating at 11.5 GHz was fabricated on an alumina substrate using silver metal, and the OI was glass coated with ITO thin film. The microwave near-field distribution was measured with and without the metamaterial absorber. Integration of the metamaterial showed improved absorption, and a 10-times increase in sensitivity at the resonance frequency of the metamaterial was calculated. In addition, the improved sensitivity was verified by an experiment comparing the TEOIM measurement system with and without the metamaterial absorber. The results provided compelling

evidence of the significant improvement in sensitivity due to the integration of metamaterial absorbers.

In addition, using the resonance properties of the metamaterial absorber, the resonance frequency shift with changes in the dielectric environment was investigated. Based on the resonance frequency shift, the equation relating the resonance frequency and the dielectric constant of the tested material was formulated. On this basis, an innovative method for imaging a non-uniform dielectric material was developed.

TABLE OF CONTENTS

LIST OF FIGURES

CHAPTER 1

Introduction

As applications for microwave (MW) near-field imaging technologies expand, they are becoming increasingly important. These technologies are now fundamental in several fields, including materials testing, monolithic microwave integrated circuit (MMIC) design, semiconductor device design, nondestructive detection, and medical diagnosis.[1]– [3] As this application landscape continues to grow, so does the need for the development of sensitive measurement methods and innovative techniques.

Thermoelastic optical indicator microscopy (TEOIM) is a new technology to measure microwave near field distribution. It is a non-destructive method that relies on the absorption properties of the thin film of an optical indicator. The optical indicator is a fundamental component of the TEOIM system, comprising a glass substrate coated with thin films. It plays a vital role in converting microwave signals into optical signals, facilitating the visualization and measurement of microwave near-field distributions[4]

The pursuit of further improvement of measurement sensitivity of TEOIM has led to an exploration of methods that improve microwave absorption within the thin film of the optical indicator. Additionally, it seeks to propose innovative approaches to characterize dielectric materials, with a particular focus on spatially varying dielectric properties. This dissertation is dedicated to this endeavor, and it is structured as follows.

1.1 Motivation

The desire to further improve the measurement sensitivity of TEOIM has led to the exploration of mechanisms that enhance microwave absorption in the thin film of the optical indicator through experimental analysis. The first part of the dissertation systematically examines the influence of varying the thickness of the thin films within the optical indicator on microwave absorption. The second part delves into the integration of metamaterial absorbers with the optical indicator.

Metamaterials, known for their ability to manipulate electromagnetic waves and enhance the absorption, are employed to explore their potential to further enhance microwave absorption. These engineered materials offer unique electromagnetic properties not found in natural materials, exhibiting an electromagnetic response attributed to their geometry[5]– [8]. They allow coupling to the radiation from free space at resonance frequency and enhance the absorption of microwaves. This property led to enhanced absorption of thin films when they are integrated with metamaterial absorbers. In TEOIM this enhanced absorption leads to a notable improvement in measurement sensitivity.

Moreover, the integration of metamaterials not only enhances sensitivity but also brings additional benefits. In the final part of this work, the frequency shift response of the metamaterial in response to variations in dielectric constants is utilized, enabling the development of an innovative method for mapping the relative permittivity of dielectric materials. This not only advances our understanding but also opens new possibilities for research and applications within this field.

1.2 Microwave Absorption and Heating Mechanism of Thin film.

When electromagnetic waves encounter a medium, the waves may be reflected, absorbed, transmitted, or any combination of these three interactions. Microwave heating is governed by two key mechanisms: dielectric heating and eddy current loss. Understanding these mechanisms is vital to utilizing the potential of microwave technology for various processes.

Dielectric heating: electric field component is responsible for this and primarily causes dielectric heating. This phenomenon involves two primary mechanisms: dipolar polarization and ionic conduction. In the presence of an oscillating electric field, dipoles in the material attempt to align but are prevented from doing so by their reaction delay, resulting in collisions and the generation of heat [9], [10].

Eddy Current Loss: Eddy current loss, on the other hand, is associated with the magnetic field component of microwaves. It arises from the induction of eddy currents within conductive materials when exposed to a changing magnetic field. The intensity of eddy current loss is closely related to the electrical resistance of the material. This mechanism is especially significant in the heating of conductors and semiconductors [9]–[13]

1.3 Factors Affecting Microwave Heating Efficiency

Several factors can affect microwave heating efficiency. One significant factor that affects the efficiency of microwave heating of thin films is the material properties of the film itself [10], [14]. Different materials have different properties, which determine their ability to absorb microwave radiation and convert it into heat. In addition, the thickness of the thin film also plays a crucial role in microwave heating efficiency. Thin films with a thickness that is comparable to the penetration depth of microwave radiation can efficiently absorb and convert microwave energy into heat[13]. Other factors that can affect the efficiency of microwave heating of thin films include the power and frequency of the microwave radiation [10], [14].. Microwave Frequency and Power play a crucial role in the heating mechanisms

of thin films. The frequency of the microwave radiation determines the depth of penetration into the film, with higher frequencies resulting in shallower penetration. This is due to higher-frequency microwaves having shorter wavelengths. In terms of power, increasing the power of the microwave radiation leads to more efficient and rapid heating of thin films. The power directly affects the rate at which the molecules in the film absorb the microwave energy, leading to an increase in temperature. Therefore, the choice of microwave frequency and power is crucial in optimizing the heating efficiency of thin films.

1.4 Optical Indicators

The optical indicator consists of a glass substrate coated with thin films. The thin film is heated by the absorption of microwaves. The specific nature of this heat generation depends on the properties of the thin-film coating. When the thin film is dielectric, it absorbs the dielectric component of the electromagnetic wave, resulting in heat production. Conversely, if the thin film is conductive, it absorbs the magnetic component of the electromagnetic wave, leading to heat generation. Based on these, the OI determines the selective measurement of electric and magnetic fields. The glass substrate is used to quantify the heat generated by the thin film using the photoelsatic effect.

The photoelastic effect is a phenomenon that occurs in certain materials when they are subjected to stress. Under stress, these materials exhibit birefringence, changing the polarization state of incident light as it passes through them. These changes in polarization can be observed and analyzed using optical techniques. Figure 1.1 (b) shows the illustration of the OI. Where the incident light generates heat and the heat generated diffuses to the glass substrate and that induces stress in glass medium

By configuring optical components as shown in Figure 1.1 (a), the intensity of the light is then measured as it passes through the analyzer due to the change in polarization state, this arrangement allows measurement of both minimum and maximum light intensity at a 45-degree angle, facilitating detection and analysis of stress-induced changes in polarization[4]

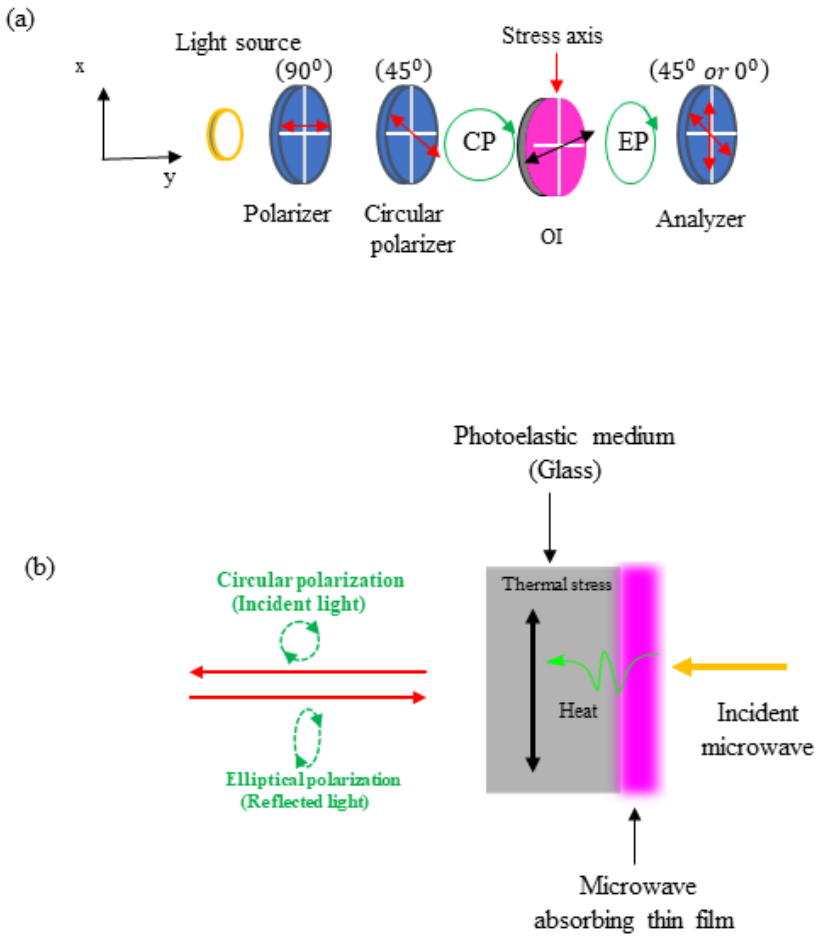

Figure 1.1. (a) **Illustration of measurement setup of the optical component to obtain the optical signal. b. Optical indicator.**

1.5 Statement of the Specific Research Objectives and Aims:

The goal of this research is to investigate and develop methods that improve the measurement sensitivity of thermoelastic optical indicator microscopy (TEOIM) and to propose applications for this technique. To achieve this overarching objective, the research is guided by the following specific objectives:

1. **Investigation of Thin Film Thickness Effects on Microwave Absorption and TEOIM Sensitivity Enhancement:**
    - Explore the correlation between the thickness of thin films and their microwave absorption properties.
    - Understand how varying film thickness impacts microwave absorption and, subsequently, enhances TEOIM sensitivity.
2. **Integration of Metamaterials with OI for Microwave Absorption Enhancement and TEOIM Sensitivity:**
    - To design and configure the metamaterial absorber with the OI to facilitate improved microwave absorption of the thin films of the OI.
    - To achieve enhanced TEOIM sensitivity through the strategic integration of metamaterials into the OI
3. **Development of a Novel Dielectric Permittivity Mapping Technique:**
    - Incorporate metamaterial absorbers into TEOIM to offer a unique mapping technique that provides insight into the electrical properties of non-homogeneous materials.
    - To advance TEOIM capabilities, making it a more effective tool for non-destructive testing and comprehensive material characterization.

1.8. Reference

[1] Z. Wang, E. G. Lim, Y. Tang, and M. Leach, “Medical applications of microwave imaging,” *Scientific World Journal*, vol. 2014, 2014, doi: 10.1155/2014/147016.

[2] B. Yang, G. Du, Y. Dong, G. Liu, Z. Hu, and Y. Wang, “Non-Invasive Imaging Method of Microwave Near Field Based on Solid State Quantum Sensing,” 2018.

[3] A. M. de Oliveira *et al.*, “A high directive Koch fractal Vivaldi antenna design for medical near-field microwave imaging applications,” *Microw Opt Technol Lett*, vol. 59, no. 2, pp. 337–346, Feb. 2017, doi: 10.1002/mop.30293.

[4] H. Lee, S. Arakelyan, B. Friedman, and K. Lee, “Temperature and microwave near field imaging by thermo-elastic optical indicator microscopy.”

[5] X. Liu, F. Xia, M. Wang, J. Liang, and M. Yun, “Working Mechanism and Progress of Electromagnetic Metamaterial Perfect Absorber,” *Photonics*, vol. 10, no. 2. MDPI, Feb. 01, 2023. doi: 10.3390/photonics10020205.

[6] Q. Huang, G. Wang, M. Zhou, J. Zheng, S. Tang, and G. Ji, “Metamaterial electromagnetic wave absorbers and devices: Design and 3D microarchitecture,” *J Mater Sci Technol*, vol. 108, pp. 90–101, May 2022, doi: 10.1016/j.jmst.2021.07.055.

[7] Y. I. Abdulkarim *et al.*, “A Review on Metamaterial Absorbers: Microwave to Optical,” *Frontiers in Physics*, vol. 10. Frontiers Media SA, Apr. 29, 2022. doi: 10.3389/fphy.2022.893791.

[8] D. Kundu, A. Mohan, and A. Chakraborty, “Ultrathin polarization independent absorber with enhanced bandwidth by incorporating giusepe peano fractal in square ring,” *Microw Opt Technol Lett*, vol. 57, no. 5, pp. 1072–1078, May 2015, doi: 10.1002/mop.29020.

[9] J. Sun, W. Wang, and Q. Yue, “Review on microwave-matter interaction fundamentals and efficient microwave-associated heating strategies,” *Materials*, vol. 9, no. 4. MDPI AG, 2016. doi: 10.3390/ma9040231.

[10] D. S. Aherrao, C. Singh, and A. K. Srivastava, “Review of ferrite-based microwave-absorbing materials: Origin, synthesis, morphological effects, dielectric/magnetic properties, composites, absorption mechanisms, and optimization,” *Journal of Applied Physics*, vol. 132, no. 24. American Institute of Physics Inc., Dec. 28, 2022. doi: 10.1063/5.0123263.

[11] I. Huynen, “micro Investigation of Microwave Absorption Mechanisms in Microcellular Foamed Conductive Composites,” 2021, doi: 10.3390/micro.

[12] D. El Khaled, N. Novas, J. A. Gazquez, and F. Manzano-Agugliaro, “Microwave dielectric heating: Applications on metals processing,” *Renewable and Sustainable Energy Reviews*, vol. 82. Elsevier Ltd, pp. 2880–2892, Feb. 01, 2018. doi: 10.1016/j.rser.2017.10.043.

[13] M. Haddadi. M, B. Das, J. Jeong, S. Kim, and D. S. Kim, “Near-maximum microwave absorption in a thin metal film at the pseudo-free-standing limit,” *Sci Rep*, vol. 12, no. 1, Dec. 2022, doi: 10.1038/s41598-022-23119-7.

[14] Q. Hu *et al.*, “Microwave technology: a novel approach to the transformation of natural metabolites,” *Chinese Medicine (United Kingdom)*, vol. 16, no. 1. BioMed Central Ltd, Dec. 01, 2021. doi: 10.1186/s13020-021-00500-8.

Chapter highlights

This chapter provides a comprehensive overview of thermoelastic optical indicator microscopy (TEOIM) and describes its components, advantages, measurement principles and how the optical indicator works. It examines strategies for improving microwave absorption in the optical indicator and discusses the measurement sensitivity of TEOIM. In addition, this chapter introduces the concept of metamaterials and their role in achieving perfect absorption. Research gaps are identified, particularly in the area of TEOIM and the integration of metamaterials, opening doors for future investigations and potential applications in this area.

CHAPTER 2

An overview of TEOIM and metamaterials

2.1 Thermoelastic Optical indicator Microscopy (TEOIM)

Thermoelastic optical indicator microscopy (TEOIM) is a technique for high-resolution imaging of microwave near-field distributions. It uses an optical indicator and a microscope system with a CCD camera. The measurement principle is based on the reconstruction of the heat source distribution from the thermal stress distribution obtained by photoelastic measurement of the optical indicator. The optical indicator (OI) consists of a glass substrate coated with a thin film that absorbs an electromagnetic (EM) field emitted from the material under investigation.

TEOIM offers several advantages, including the use of conventional materials and equipment, and real-time measurement capability. It has been successfully used for various NDT applications, such as monitoring electronic devices during operation, characterization and crack detection of conductive thin films, inspection of conductive particles embedded in opaque dielectric materials, non-invasive measurement of liquid concentrations, and defect detection in dielectric materials.[1]– [4]

2.2 Components of TEOIM

The components of Thermo-Elastic Optical Indicator Microscopy (TEOIM) include an Optical Indicator (OI), a polarized light microscope system consisting of polarizers, and a CCD camera. The OI is a thin film coated on the glass substrate that absorbs the electromagnetic radiation from the Device Under Test (DUT) and undergoes a change in its optical properties.

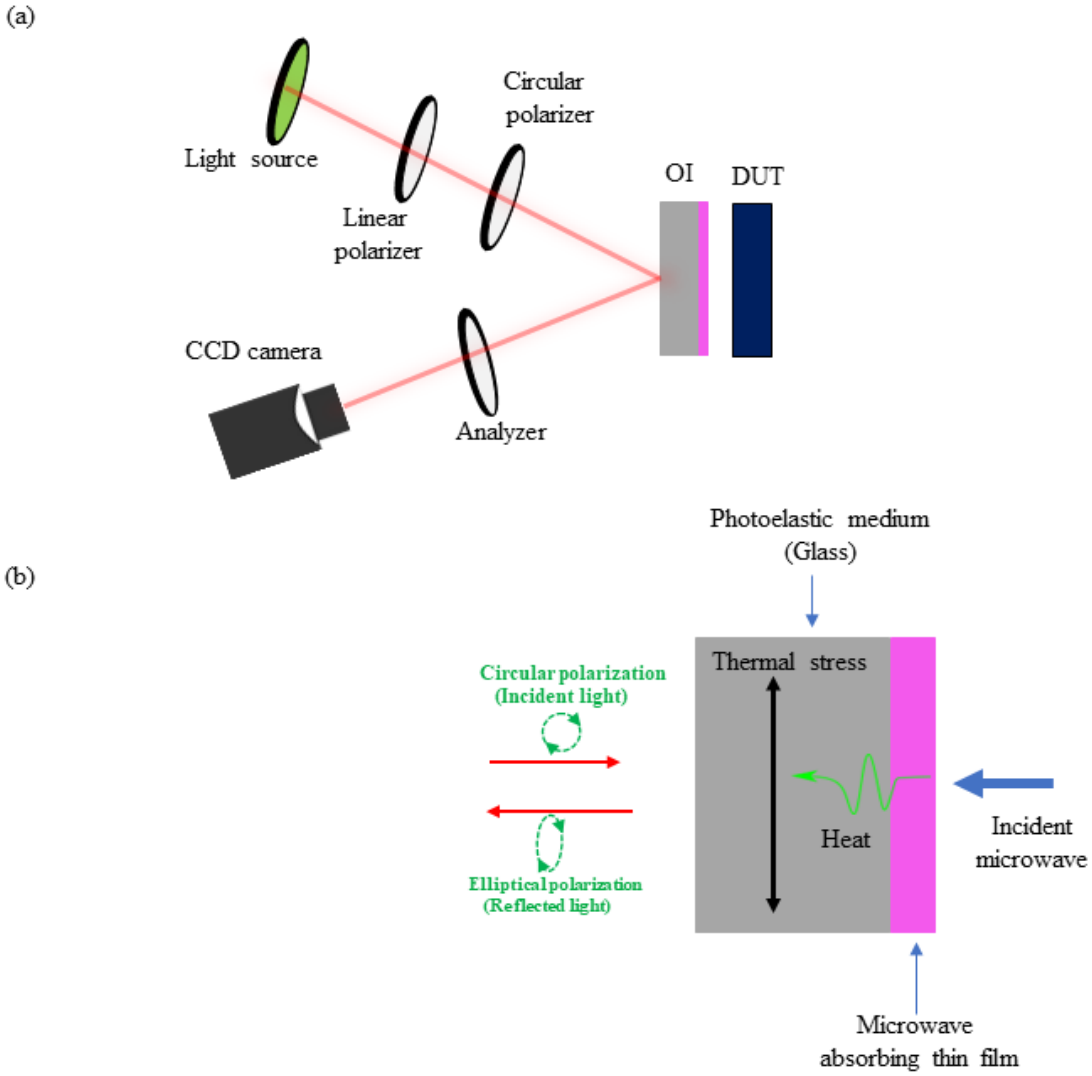

Figure 2.1 (a) experimental setup of TEOIM (b) measurement principle of TEOIM

The polarized light microscope system is used to visualize and analyze the changes in the polarization state and intensity of the light transmitted through the OI material. It includes components such as a light source and polarizers. The linear polarizer changes the light from the light source to linear polarization and circular polarizers change the light from linear polarization to circular polarization, and the sheet polarizer is used to analyze the polarization state of the reflected light.

The CCD camera is used to capture the intensity changes of the transmitted light passing through the OI material. It records the images of the OI material and allows for real-time

visualization and analysis of the microwave near-field distribution. These components work together to enable the measurement and visualization of the microwave near-field distribution in TEOIM.[5]

2.3 The existing optical indicators utilized in TEOIM.

Various types of optical indicators are reported in the literature; for instance, to measure the electric near field, a sliding glass coated with aluminum nanoparticles (AlNP) embedded in a poly (methyl methacrylate) (PMMA) thin film was used as the optical indicator (OI) material to measure the microwave electric component, and a conductive platinum (Pt) thin film with a thickness of 200 nm was used as the OI material for measuring the microwave magnetic near-field[4]. ITO-based optical indicators are used in various applications of non-destructive measurements by using TEOIM[1]–[3], [6]. Additionally, new types of optical indicators called meta-surface-based optical indicator was reported to measure the electrical microwave fields[7].

2.4 Measuring principle of TEOIM

The principle of thermoelastic optical indicator microscopy (TEOIM) is based on the measurement of the thermal stress distribution in an optical indicator (OI) caused by the absorption of the microwave signal radiated from the DUT. This absorption generates heat, which then diffuses into the glass substrate of the OI, resulting in a thermal stress distribution within the glass substrate.

The stressed OI material exhibits the photoelastic effect, where the polarization state of incident light passing through the material is changed into an elliptically polarized state, depending on the stress axis and material properties. This change in polarization state can be measured by monitoring the linear birefringence (LB) of the OI material. By analyzing the

change in LB of the OI material, the heat source distribution visualized [5]. The measurement setup and measurement principle are shown in Figure 2.1

2.5 Strategies for Enhancing Microwave Signal Absorption in Thin Films and its application for OI.

There are numerous strategies to improve the microwave absorption of thin films. One of them is the incorporation of additives into the thin films [8]– [11]. This strategy has been applied in the context of the optical indicator (OI) in TEOIM [5]. Aluminum nanoparticles have been used due to their high absorption coefficient, which makes them suitable for measuring electric microwave fields.

Another effective strategy is to optimize the thickness of the metal thin film itself to increase absorption [12]– [14]. While these strategies have been used in optical indicator applications. Recent developments have demonstrated the potential of metamaterial absorbers integrated into thin films to enhance microwave absorption [15]– [22]. However, its application in the context of OI absorption is still relatively unexplored.

2.6 Measuring sensitivity of TEOIM

The sensitivity of TEOIM is important for understanding its performance in detecting microwave fields. This sensitivity is determined by the relationship between microwave field intensity and the absorption of an optical indicator (OI). Essentially, when microwaves are absorbed by the OI, it generates heat, resulting in changes in its optical properties. These changes lead to alterations in the intensity of light passing through the indicator material, making it a measurable parameter for quantifying microwave absorption.[4],

Practically, the sensitivity of TEOIM is assessed by calculating the change in response to incident microwave power. In the study conducted by [4], the sensitivity of the indicators to

incident microwave power was determined by analyzing the change in intensity (ΔI) to the change in microwave power (ΔP), and it is defined as follows.

$$S = \Delta I / \Delta P \qquad 2.1$$

The researchers plotted the calculated intensity changes as a function of incident microwave power. Through this comparison, they quantified the sensitivity by assessing how the change in intensity relates to the incident power. In particular, at a microwave frequency of 10 GHz, predictable sensitivities ranged from 0.1 to 1 mW for measurements averaged over 15,000 times. Notably, the intensity of light passing through the OI material exhibited a linear increase with an increase in the incident microwave power [4].

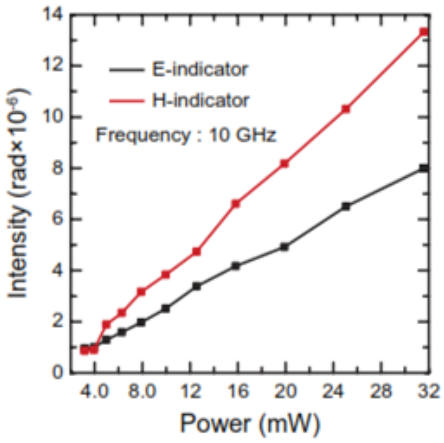

Figure 2.2 Calculated average intensities of electric (black) and magnetic (red) fields at 10GHz as a function of incident microwave power[4]

This relationship between absorption and incident power was consistently demonstrated for both electric and magnetic fields. Figure 2.5 in the study visually depicts the calculated intensity changes as a function of incident microwave power at 10 GHz. The graphical representation of the data clearly illustrates the linear increase in intensity changes for both the electric and magnetic fields.

2.7 Metamaterials

Metamaterials are man-made materials that usually have periodically arranged structures with dimensions smaller than the wavelength of the desired operating frequency. They exhibit electromagnetic properties that differ significantly from those of naturally occurring materials. Metamaterials derive their properties from a combination of composition and structure rather than from their composition alone[23]– [26]. The existence of metamaterials was first foreseen by Victor Veselago, a Russian physicist, in his pioneering research on the existence of materials with negative refractive index. He described their properties decades before their physical realization. The theoretical background of metamaterials begins with Maxwell's laws of electromagnetism [27]. For an electromagnetic (EM) time-harmonic wave propagating in a lossy medium with conductivity σ, dielectric constant ε, and permeability μ, four laws are given in differential form by.

$$\nabla . E = 0 \quad (2.2)$$

$$\nabla . H = 0 \quad (2.3)$$

$$\nabla \times E = -j\omega\mu H \quad (2.4)$$

$$\nabla \times H = (\sigma + j\omega\varepsilon)E \quad (2.5)$$

Applying curls on both sides of the equation on equation 3 for the waves in lossy dielectric the electric field becomes.

$$\nabla^2 E + \gamma^2 E = 0 \quad (2.6)$$

where, $\gamma^2 = \sqrt{j\omega\mu(\sigma + j\omega\varepsilon)}$ the propagation constant

Similarly, the magnetic field can be written as

$$\nabla^2 H + \gamma^2 H = 0 \qquad 2.7$$

The above equations are Helmholtz equations.

If the wave plane monochromatic wave travels in the z direction the electric and the magnetic fields are prospecting along the x and y direction, respectively.

Then the above equation can be simplified further

$$E = E_x(z)a_x \qquad 2.8$$

$$E_x(z) = E_0 e^{\gamma z} + E'_0 e^{-\gamma z} \qquad 2.9$$

$$E(z,t) = Real(E_x(z)a_x e^{j\omega t}) \qquad 2.10$$

As γ is a complex number it can be represented by

$$\gamma = \alpha + j\beta \qquad 2.11$$

Thus

$$E(z,t) = E_0 e^{-\alpha z} cos(\omega t - kz)a_x \qquad 2.12$$

Similarly, the magnetic field

$$H(z,t) = H_0 e^{-\alpha z} cos(\omega t - kz)a_x \qquad 2.13$$

The relation between the two becomes.

$$H_0 = {}^{E_0}/_{\eta} \qquad 2.14$$

If the medium is lossless the conductivity is approximately zero, and thus the E field and the H field are in phase with one another.

The permittivity (ε) and permeability (μ) of a medium affect the propagation of the electromagnetic wave shown in Figure 2.3 The first group of material is named double positive material, as both permittivity and permeability of the material are greater than zero. This category primarily contains dielectrics. Permittivity is less than zero and permeability is larger than zero in the second category, which is why it is termed epsilon negative material. Many plasmas exhibit these properties at certain frequency regimes. The third group of materials possesses a permittivity greater than zero and permeability less than zero. Gyro tropic magnetic materials display these characteristics and are called mu-negative materials. The fourth group contains the double negative material, which can only be produced artificially. This class of material has both permittivity and permeability less than zero, or negative. When an EM wave enters such media, the direction of wave propagation reverses. No naturally available material has both negative permeability and permittivity[25].

2.8 Metamaterial Absorbers

The field of metamaterials has made significant progress in recent years, with a particular class of materials known as metamaterial absorbers attracting considerable attention. Metamaterial absorbers have become a promising area of research due to their unique properties. They have applications in several areas, such as reducing the radar cross section (RCS) of targets, improving detection capabilities, and reducing the side lobes of antennas. Typically, they are structured as 2-D meta surfaces consisting of an array of unit cells (n×n). These unit cells are carefully designed to match the impedance of the entire structure to that of free space. When an electromagnetic wave of a certain frequency hits the metamaterial

absorber, it induces electrical and magnetic excitations at that frequency, resulting in absorption.

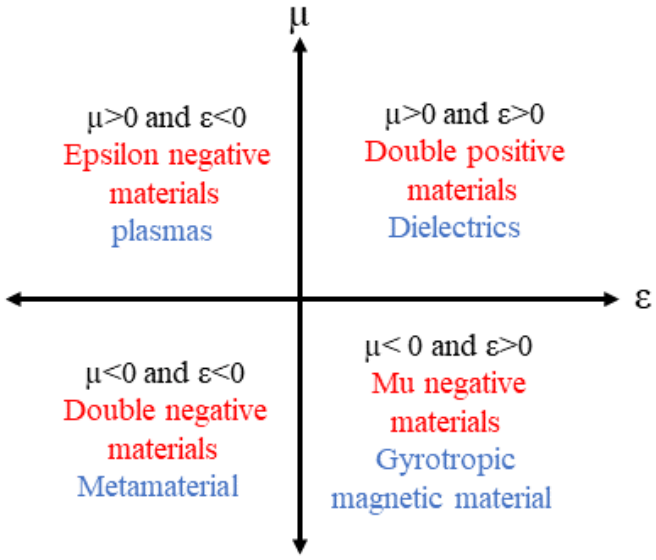

Figure 2.3 Classification of materials

A crucial mechanism by which metamaterial absorbers can achieve perfect absorption is the technique of impedance matching. In this approach, the metamaterial absorber is designed to have an impedance equal to that of the incident electromagnetic wave, minimizing reflection and maximizing absorption.

Another key element contributing to the perfect absorption mechanism in metamaterial absorbers is their electromagnetic resonance-based absorption. This mechanism is based on the resonant interaction between the incident electromagnetic wave and the structural components of the metamaterial absorber. Specially designed, periodically arranged metal layers create specific resonances at the desired frequency. To achieve impedance matching to free space, the dimensions of these resonators must be adjusted. Under this condition of impedance matching, the reflectivity on the device disappears and ensures that all incident EM waves are efficiently coupled into the absorber.

2.9 General principles of the absorption mechanism metamaterial

When an electromagnetic wave incident on a structure, it can be reflected, transmitted, or absorbed. An electromagnetic absorber can avoid reflection and transmission, converting all the incoming energy into thermal energy through dissipation. To describe this phenomenon, the energy law is introduced by.

$$A = 1 - R - T \tag{2.15}$$

where A is the absorbance, R is the reflectance, and T is the transmittance. The absorbers are bounded by a metallic plate at the bottom that cancels all transmission, which means T = 0, reducing

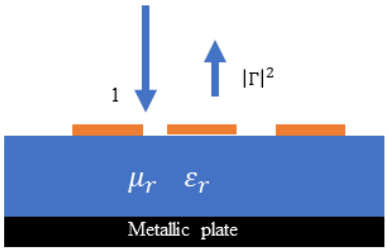

Figure 2.4 The geometry of a metamaterial. Here blocks indicating resonators. 1 is the unitary incident power that can be either reflected or absorbed. The metallic plate assures zero transmission.

$$A = 1 - R \tag{2.16}$$

Thus, to obtain total absorption, the condition of zero reflection is required. This condition is known as impedance matching.

To understand the impedance matching condition, we assume the case of a plane wave traveling in free space under normal incidence and reaching a medium above a metal plate, as depicted in Figure 2.4.

Let R is the reflectance corresponding to the power ratio between the reflected and incident waves. It can be written in terms of complex reflection coefficient Γ, or complex reflection

coefficient described by the scattering parameter S11, both Γ and S_{11} are expressed as voltage ratios.

$$R = |\Gamma|^2 \quad 2.17$$

$$R = |S_{11}|^2 \quad 2.18$$

$$A = 1 - |S_{11}|^2 = 1 - |S_{11}|^2 \quad 2.19$$

$$\Gamma = \frac{\eta - \eta_0}{\eta + \eta_0} \quad 2.20$$

Since the transmission is zero below the metal plate, the unitary absorptivity described is achieved through material losses when the reflection coefficient in the equation vanishes.

where η is the intrinsic impedance of the medium and η_0 is the intrinsic impedance of the free space (air) equal to 377 Ω. When $\eta = \eta_0$, the impedance matching condition is satisfied since the reflection coefficient (Γ) is zero. The intrinsic impedance of a generic material η is dependent only on the constitutive parameters of the medium. where μ and ε are complex values corresponding to the permeability and permittivity, respectively, and are described by equation.

$$\eta = \sqrt{\frac{\mu}{\varepsilon}} = \sqrt{\frac{\mu_0 \mu_r}{\varepsilon_0 \varepsilon_r}} = \mu_0 \sqrt{\frac{\mu_r}{\varepsilon_r}} \quad 2.21$$

The metamaterial unit structure is artificially designed to equate ε and μ to satisfy the impedance matching relation in Equation 2.21. where η is the wave impedance of the material and η_0 is the wave impedance in the free space. The appropriate impedance matching will make all the incident waves enter the absorber structure without reflection, and the energy loss is contributed by the imaginary part of the complex equivalent ε and μ. By designing the imaginary part, the energy can be dissipated to the maximum extent, reducing transmission and reflection, and finally achieving perfect wave absorption.

2.10 Integration of optical indicators (OI) with metamaterial absorbers

Studies have demonstrated that the integration of metamaterial absorbers can enhance the absorption performance of thin films[28]– [32]. However, the potential for improving the absorption capabilities of OI through the integration of metamaterials remains unexplored. This research is dedicated to exploring the integration of an OI with a metamaterial absorber, presenting a new approach expected to enhance microwave absorption within the thin films of the OI. This integration promises to improve the measurement sensitivity of Thermoelastic Optical Indicator Microscopy (TEOIM). It utilizes the principles of microwave absorption of thin films with the resonance effect of metamaterial. This integration encompasses both theoretical and practical dimensions.

The theoretical aspect of integrating an OI with a metamaterial absorber depends on the understanding of the electromagnetic properties of both components. The Optical Indicator, known for its capacity to absorb microwave signals and convert them into optical signals, is combined with a metamaterial absorber. This absorber enhances the absorption of electromagnetic waves through its resonance effects. The conceptual framework for the metamaterial integrated and without metamaterial integrated system is explained in Figure 2.5. When the optical indicator is exposed to the microwave near field or incident microwave radiation, absorption leads to heating. The heat generated by the microwave depends on the loss property of the material coated on the glass substrate. For the case where the glass substrate is coated with a dielectric loss material, the generated heat by the dielectric loss per unit volume is as follows[33].

$$\mathbf{q} = \frac{\omega}{2}\varepsilon''|\mathbf{E}|^2 \qquad 2.22$$

Conversely, for the metamaterial integrated approach, the heat generated by the OI can be expressed as

$$q_{enhanced} = \frac{\omega}{2}\varepsilon''|\mathbf{E}|^2 \qquad 2.23$$

And

When the conductive metal thin film is coated on the glass substrate, the resistive losses (or ohmic losses) are responsible for generating heat. Then, the absorbed microwave by the thin metal film is.

$$q = \frac{P_{av}}{V} = \frac{R_s}{2t}|\mathrm{H}|^2 \qquad 2.24$$

Where H is the microwave magnetic field tangential to the surface of the thin metal film, R_s and δ_s are the surface resistivity and skin depth of the metal-thin film, respectively. In the same way for the metamaterial integrated system, the above equation becomes.

$$q_{enhanced} = \frac{P_{av}}{V} = \frac{R_s}{2t}|\mathrm{H}|^2 \qquad 2.25$$

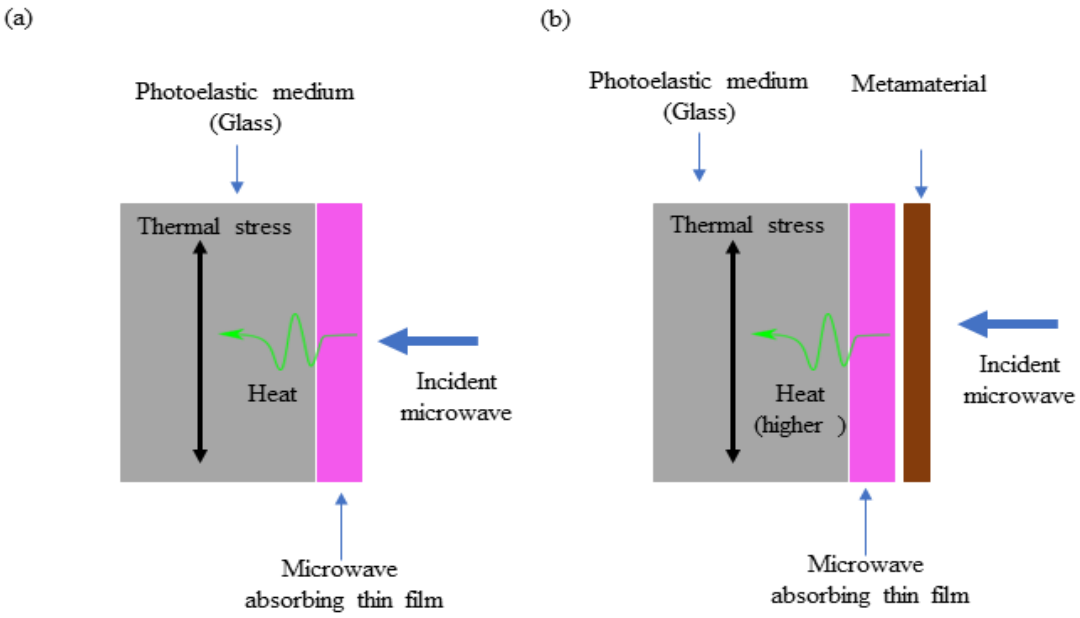

Figure 2.5 Illustration of OI (a) without metamaterial (b) with metamaterial integrated.

In any case, the generated heat is diffused to the glass substrate due to thermal conduction, the temperature change of the glass substrate can be expressed as.

$$-\left(K\nabla^2 T\right) = q \tag{2.26}$$

This heat distribution on the optical indicator can be visualized using probing polarized light and a CCD camera. Importantly, the heat distribution on the optical indicator is directly proportional to the microwave near-field distribution. Areas of high microwave intensity exhibit increased absorption and heating in the metal film, resulting in localized temperature variations that are captured by the optical indicator [33]. The heat source distribution on the optical indicator was calculated as [33].

$$q = C\frac{\partial^2 \beta_2(x,y)}{\partial x \partial y} + \frac{\partial^2 \beta_1(x,y)}{\partial x^2} + \frac{\partial^2 \beta_2(x,y)}{\partial y^2} \tag{2.27}$$

Where C is a constant related to the wavelength of the light, thickness, and stress optical constant of the glass substrate. Practically, β_1 and β_2 are two related to the normal and shear stress distributions of the OI and calculated from measured images with different polarization states of light and the orientations of the optical axis of the analyzer [34]

In the practical aspect, integration involves physically fabricating the Optical Indicator (OI) and metamaterial absorbers. The precise assembly of the components in the TEOIM structure is critical to ensure they work together effectively in improving microwave absorption. The selection of materials, geometries of structures, and specific design parameters play a central role in achieving the desired results.

2.11 Mapping dielectric constant with metamaterial integrated frequency shift

Metamaterial absorbers (MA) offer exciting possibilities beyond their traditional role in enhancing microwave absorption. They are becoming pivotal in the field of sensors. MA

sensors stand out for their simplicity in design, cost-effectiveness, ease of fabrication, and remarkable sensitivity, making them ideal for applications ranging from temperature and humidity measurement to assessing pressure and agricultural product quality. The key to their sensitivity lies in their capacity to detect changes in resonant frequency, which, in turn, stems from variations in the permittivity of the material under test (MUT). The quality factor of MA plays a crucial role in their sensitivity, as higher quality factors result in a narrower absorption bandwidth, leading to increased frequency selectivity. A high-sensitivity MA demands substantial absorption to confine electromagnetic fields near the structure. To achieve this, MAs are engineered with specific resonant frequencies and excited with electromagnetic fields. When the MUT interacts with this field, it alters the resonant frequency [40]– [42]. A substantial shift in resonance frequency (δf) indicates a highly sensitive MA and it's given by

$$\delta f = f_0 - f_1 \tag{2.28}$$

Where f_0 is the resonant frequency of MA sensor and f_1 is the resonant frequency of a sensor after interaction with MUT. The frequencies are calculated by.

$$f_0 = \frac{1}{2\pi\sqrt{LC}} \tag{2.29}$$

The inductance (L) and capacitance (C) of the MA sensor before interaction with the MUT determine these frequencies. Additionally, a new parameter, C_M (capacitance introduced due to the interaction of the MA sensor with the MUT), comes into play during the interaction. [43]

$$f_1 = \frac{1}{2\pi\sqrt{L(C + C_M)}} \quad 2.30$$

MA-based sensors are versatile and find applications in various sensing domains. The literature abounds with reports of MA sensors for measuring dielectric permittivity in materials exhibiting a uniform dielectric constant [43]– [48]. However, when dealing with materials featuring spatially varying dielectric constants, conventional methods become less practical. In such cases, alternative techniques like near-field scanning microwave microscopy (NSMM) and microwave holography come to the rescue [49-50]. NSMM involves systematically scanning a probe tip over the sample surface to create images of the local electromagnetic field. This method provides a high-resolution representation of dielectric properties. On the other hand, microwave holography leverages interference patterns generated by microwaves reflected from or transmitted through the sample to reconstruct the distribution of dielectric permittivity. Nonetheless, the scanning approach in these methods can be time-consuming and may not suit large-scale or time-critical applications.

2.12 Research gaps in TEOIM and metamaterial absorber integration

Review of the existing literature on thermoelastic optical indicator microscopy (TEOIM) has revealed research gaps that provide opportunities for investigation and exploration. These gaps include:

1. Limited exploration of metamaterial integration: current research focuses primarily on the fundamentals of TEOIM. However, there is a significant research gap in exploring how metamaterial absorbers can be effectively integrated into TEOIM

systems. This integration represents an exciting opportunity to improve microwave absorption, and the potential applications remain largely untapped.

2. Strategies to improve sensitivity: Although various strategies to improve microwave absorption in optical indicator (OI) have been discussed, there is a lack of comprehensive research on how metamaterial absorbers, known for their unique electromagnetic properties, can be seamlessly integrated to further improve sensitivity.
3. Potential Applications: The review suggests potential applications of TEOIM integrated with metamaterials as an optical indicator for electric component imaging and characterizing the metamaterial using the TEOIM field visualization method. However, further research is needed to explore the full potential of integrating metamaterials with TEOIM. Future research should explore the practicalities of implementing this integration and identify specific use cases.
4. Dielectric constant mapping: conventional methods for mapping dielectric constants work well for uniform materials. However, there is a notable research gap in understanding how integrating metamaterial absorbers with TEOIM can effectively map spatial variations in dielectric constants. Research in this area is critical to expanding the capabilities of TEOIM.

2.13 Reference

[1] H. Lee, Z. Baghdasaryan, B. Friedman, and K. Lee, “Detection of a Conductive Object Embedded in an Optically Opaque Dielectric Medium by the Thermo-Elastic Optical Indicator Microscopy,” *IEEE Access*, vol. 7, pp. 46084–46091, 2019, doi: 10.1109/ACCESS.2019.2908885.

[2] Z. Baghdasaryan, A. Babajanyan, L. Odabashyan, J. H. Lee, B. Friedman, and K. Lee, “Visualization of microwave near-field distribution in sodium chloride and glucose aqueous solutions by a thermo-elastic optical indicator microscope,” *Sci Rep*, vol. 11, no. 1, Dec. 2021, doi: 10.1038/s41598-020-80328-8.

[3] H. Lee, Z. Baghdasaryan, B. Friedman, and K. Lee, “Electrical Defect Imaging of ITO Coated Glass by Optical Microscope with Microwave Heating,” *IEEE Access*, vol. 7, pp. 42201–42209, 2019, doi: 10.1109/ACCESS.2019.2907013.

[4] H. Lee, S. Arakelyan, B. Friedman, and K. Lee, “Temperature and microwave near field imaging by thermo-elastic optical indicator microscopy.”

[5] H. Lee, S. Arakelyan, B. Friedman, and K. Lee, “Temperature and microwave near field imaging by thermo-elastic optical indicator microscopy.”

[6] S. Hamelo, J. Yang, and H. Lee, “Detection of Defects in a Dielectric Material by Thermo-Elastic Optical Indicator Microscopy,” *IEEE Access*, vol. 11, pp. 45961–45971, 2023, doi: 10.1109/ACCESS.2023.3274534.

[7] Z. Baghdasaryan *et al.*, “3D visualization of microwave electric and magnetic fields by using a metasurface-based indicator,” *Sci Rep*, vol. 12, no. 1, Dec. 2022, doi: 10.1038/s41598-022-10073-7.

[8] S. Hoghoghifard and H. Mokhtari, “Improving the microwave absorption in Ni-coated fabrics by saccharin addition in plating bath,” *Journal of Industrial Textiles*, vol. 49, no. 3. SAGE Publications Ltd, pp. 402–411, Sep. 01, 2019. doi: 10.1177/1528083718787525.

[9] P. W. Liang *et al.*, “Additive enhanced crystallization of solution-processed perovskite for highly efficient planar-heterojunction solar cells,” *Advanced Materials*, vol. 26, no. 22, pp. 3748–3754, Jun. 2014, doi: 10.1002/adma.201400231.

[10] D. H. Kim *et al.*, “Bimolecular Additives Improve Wide-Band-Gap Perovskites for Efficient Tandem Solar Cells with CIGS,” *Joule*, vol. 3, no. 7, pp. 1734–1745, Jul. 2019, doi: 10.1016/j.joule.2019.04.012.

[11] F. Wang, C. Bai, L. Chen, and Y. Yu, “Boron nitride nanocomposites for microwave absorption: A review,” *Materials Today Nano*, vol. 13. Elsevier Ltd, Mar. 01, 2021. doi: 10.1016/j.mtnano.2020.100108.

[12] P. A. Yang *et al.*, “Optimization of Fe@Ag core–shell nanowires with improved impedance matching and microwave absorption properties,” *Chemical Engineering Journal*, vol. 430, Feb. 2022, doi: 10.1016/j.cej.2021.132878.

[13] M. Feng *et al.*, “Material-structure collaborative design for broadband microwave absorption metamaterial with low density and thin thickness,” *Compos B Eng*, vol. 263, Aug. 2023, doi: 10.1016/j.compositesb.2023.110862.

[14] D. S. Aherrao, C. Singh, and A. K. Srivastava, “Review of ferrite-based microwave-absorbing materials: Origin, synthesis, morphological effects, dielectric/magnetic properties, composites, absorption mechanisms, and optimization,” *Journal of Applied Physics*, vol. 132, no. 24. American Institute of Physics Inc., Dec. 28, 2022. doi: 10.1063/5.0123263.

[15] Y. Qi *et al.*, “A tunable terahertz metamaterial absorber composed of elliptical ring graphene arrays with refractive index sensing application,” *Results Phys*, vol. 16, Mar. 2020, doi: 10.1016/j.rinp.2020.103012.

[16] J. Gou, Q. Niu, K. Liang, J. Wang, and Y. Jiang, “Frequency Modulation and Absorption Improvement of THz Micro-bolometer with Micro-bridge Structure by Spiral-Type Antennas,” *Nanoscale Res Lett*, vol. 13, 2018, doi: 10.1186/s11671-018-2484-7.

[17] *2008 International Workshop on Metamaterials.* I E E E, 2008.

[18] S. Lai *et al.*, “A High-Performance Ultra-Broadband Transparent Absorber With a Patterned ITO Metasurface,” *IEEE Photonics J*, vol. 14, no. 3, Jun. 2022, doi: 10.1109/JPHOT.2022.3171864.

[19] H.-M. Lee and H.-S. Lee, “A METAMATERIAL BASED MICROWAVE ABSORBER COMPOSED OF COPLANAR ELECTRIC-FIELD-COUP-LED RESONATOR AND WIRE ARRAY,” 2013.

[20] Y. Zou *et al.*, “Improved microwave absorption of carbonyl iron powder by the array of subwavelength metallic cut wires,” *IEEE Journal on Selected Topics in Quantum Electronics*, vol. 16, no. 2, pp. 441–445, Mar. 2010, doi: 10.1109/JSTQE.2009.2033256.

[21] L. Pometcu, A. Sharaiha, R. Benzerga, P. Pouliguen, and G. Dun, “Improved Microwave Absorption of Pyramidal Absorber Using Metamaterial.”

[22] C. M. Watts, X. L. Liu, and W. J. Padilla, “Metamaterial Electromagnetic Wave Absorbers,” 2002.

[23] P. Yu *et al.*, “Broadband Metamaterial Absorbers,” *Advanced Optical Materials*, vol. 7, no. 3. Wiley-VCH Verlag, Feb. 05, 2019. doi: 10.1002/adom.201800995.

[24] M. Amiri, F. Tofigh, N. Shariati, J. Lipman, and M. Abolhasan, “Review on Metamaterial Perfect Absorbers and Their Applications to IoT,” *IEEE Internet of Things Journal*, vol. 8, no. 6. Institute of Electrical and Electronics Engineers Inc., pp. 4105–4131, Mar. 15, 2021. doi: 10.1109/JIOT.2020.3025585.

[25] Y. I. Abdulkarim *et al.*, “A Review on Metamaterial Absorbers: Microwave to Optical,” *Frontiers in Physics*, vol. 10. Frontiers Media SA, Apr. 29, 2022. doi: 10.3389/fphy.2022.893791.

[26] W. Li, M. Xu, H. X. Xu, X. Wang, and W. Huang, “Metamaterial Absorbers: From Tunable Surface to Structural Transformation,” *Advanced Materials*, vol. 34, no. 38. John Wiley and Sons Inc, Sep. 01, 2022. doi: 10.1002/adma.202202509.

[27] “YEE: SOLUTION OF INITIAL BOUNDARY VALUE PROBLEMS.”

[28] Y. Qi *et al.*, "A tunable terahertz metamaterial absorber composed of elliptical ring graphene arrays with refractive index sensing application," *Results Phys*, vol. 16, Mar. 2020, doi: 10.1016/j.rinp.2020.103012.

[29] J. Gou, Q. Niu, K. Liang, J. Wang, and Y. Jiang, "Frequency Modulation and Absorption Improvement of THz Micro-bolometer with Micro-bridge Structure by Spiral-Type Antennas," *Nanoscale Res Lett*, vol. 13, 2018, doi: 10.1186/s11671-018-2484-7.

[30] L. Pometcu, A. Sharaiha, R. Benzerga, P. Pouliguen, and G. Dun, "Improved Microwave Absorption of Pyramidal Absorber Using Metamaterial."

[31] C. M. Watts, X. L. Liu, and W. J. Padilla, "Metamaterial Electromagnetic Wave Absorbers," 2002.

[32] H.-M. Lee and H.-S. Lee, "A METAMATERIAL BASED MICROWAVE ABSORBER COMPOSED OF COPLANAR ELECTRIC-FIELD-COUP-LED RESONATOR AND WIRE ARRAY," 2013.

[33] H. Lee, S. Arakelyan, B. Friedman, and K. Lee, "Temperature and microwave near field imaging by thermo-elastic optical indicator microscopy."

[34] E. Pert *et al.*, "Temperature Measurements during Microwave Processing: The Significance of Thermocouple Effects," *Journal of the American Ceramic Society*, vol. 84, no. 9, pp. 1981–1986, 2001, doi: 10.1111/j.1151-2916.2001.tb00946.x.

[35] Z. Baghdasaryan, A. Babajanyan, L. Odabashyan, J. H. Lee, B. Friedman, and K. Lee, "Visualization of microwave near-field distribution in sodium chloride and glucose aqueous solutions by a thermo-elastic optical indicator microscope," *Sci Rep*, vol. 11, no. 1, Dec. 2021, doi: 10.1038/s41598-020-80328-8.

[36] H. Lee, Z. Baghdasaryan, B. Friedman, and K. Lee, "Electrical Defect Imaging of ITO Coated Glass by Optical Microscope with Microwave Heating," *IEEE Access*, vol. 7, pp. 42201–42209, 2019, doi: 10.1109/ACCESS.2019.2907013.

[37] Z. Baghdasaryan, A. Babajanyan, L. Odabashyan, J. H. Lee, B. Friedman, and K. Lee, "Visualization of microwave near-field distribution in sodium chloride and glucose aqueous solutions by a thermo-elastic optical indicator microscope," *Sci Rep*, vol. 11, no. 1, Dec. 2021, doi: 10.1038/s41598-020-80328-8.

[38] S. Hamelo, J. Yang, and H. Lee, "Detection of Defects in a Dielectric Material by Thermo-Elastic Optical Indicator Microscopy," *IEEE Access*, vol. 11, pp. 45961–45971, 2023, doi: 10.1109/ACCESS.2023.3274534.

[39] H. Lee, Z. Baghdasaryan, B. Friedman, and K. Lee, "Detection of a Conductive Object Embedded in an Optically Opaque Dielectric Medium by the Thermo-Elastic Optical Indicator Microscopy," *IEEE Access*, vol. 7, pp. 46084–46091, 2019, doi: 10.1109/ACCESS.2019.2908885.

[40] Y. Zhang, J. Zhao, J. Cao, and B. Mao, "Microwave metamaterial absorber for non-destructive sensing applications of grain," *Sensors (Switzerland)*, vol. 18, no. 6, Jun. 2018, doi: 10.3390/s18061912.

[41] M. A. H. Ansari, A. K. Jha, and M. J. Akhtar, "Design and Application of the CSRR-Based Planar Sensor for Noninvasive Measurement of Complex Permittivity," *IEEE Sens J*, vol. 15, no. 12, pp. 7181–7189, Dec. 2015, doi: 10.1109/JSEN.2015.2469683.

[42] M. S. Boybay and O. M. Ramahi, "Material characterization using complementary split-ring resonators," *IEEE Trans Instrum Meas*, vol. 61, no. 11, pp. 3039–3046, 2012, doi: 10.1109/TIM.2012.2203450.

[43] D. Isakov, C. J. Stevens, F. Castles, and P. S. Grant, "A Split Ring Resonator Dielectric Probe for Near-Field Dielectric Imaging," *Sci Rep*, vol. 7, no. 1, Dec. 2017, doi: 10.1038/s41598-017-02176-3.

[44] A. Soffiatti, Y. Max, S. G. Silva, and L. M. de Mendonça, "Microwave metamaterial-based sensor for dielectric characterization of liquids," *Sensors (Switzerland)*, vol. 18, no. 5, May 2018, doi: 10.3390/s18051513.

[45] Y. Zhang, J. Zhao, J. Cao, and B. Mao, “Microwave metamaterial absorber for non-destructive sensing applications of grain,” *Sensors (Switzerland)*, vol. 18, no. 6, Jun. 2018, doi: 10.3390/s18061912.

[46] T. ul Haq, C. Ruan, X. Zhang, and S. Ullah, “Complementary Metamaterial Sensor for Nondestructive Evaluation of Dielectric Substrates,” *Sensors*, vol. 19, no. 9, May 2019, doi: 10.3390/s19092100.

[47] Q. Huang, G. Wang, M. Zhou, J. Zheng, S. Tang, and G. Ji, “Metamaterial electromagnetic wave absorbers and devices: Design and 3D microarchitecture,” *J Mater Sci Technol*, vol. 108, pp. 90–101, May 2022, doi: 10.1016/j.jmst.2021.07.055.

[48] Y. Cao, K. Chen, and C. Ruan, “A Microwave Metamaterial-inspired Sensor for Nondestructive Evaluation of Dielectric Substrates,” in *2021 International Conference on Microwave and Millimeter Wave Technology, ICMMT 2021 - Proceedings*, Institute of Electrical and Electronics Engineers Inc., 2021. doi: 10.1109/ICMMT52847.2021.9617917.

[49] A. Ahmed, V. Kumari, and G. Sheoran, “Non-Destructive Dielectric Measurement and Mapping Using Microwave holography,” in *2022 2nd Asian Conference on Innovation in Technology, ASIANCON 2022*, Institute of Electrical and Electronics Engineers Inc., 2022. doi: 10.1109/ASIANCON55314.2022.9909059.

[50] IEEE Electrical Insulation Society Staff, *2013 13th Mediterranean Microwave Symposium (MMS)*. IEEE, 2013.

Chapter highlights

This chapter introduces the key elements of the experiment and simulation that have been used in this thesis. It covers the instrumentation and measurement setup of the TEOIM, including the generation and amplification of microwave signals, and the fabrication of metamaterials. It also explains the materials used in fabrication and their properties and characteristics. In addition, the chapter includes an explanation of the experimental procedures and techniques.

CHAPTER 3

Materials Method and measuring technique.

3.1 Instrumentation and Measurement Setup of TEOIM

Figure 3.1 illustrates the three sections of the Thermoelastic Optical Indicator Microscopy (TEOIM) system. It comprises the microwave section (right section of Figure 3.1), the optical section (left section of Figure 3.1), and the optical indicator. In the microwave section, a microwave signal is generated and amplified to the required power level. This signal is then connected to the antennas using coaxial cables.

The optical section of TEOIM includes a light source, polarizers, and an imaging system. This section plays a vital role in controlling the light path, manipulating the polarization state of the incident light, and capturing optical signals for visualization and analysis. The optical indicator is positioned between the microwave section and the optical section. Its function is to absorb microwave radiation and convert it into a measurable optical signal.

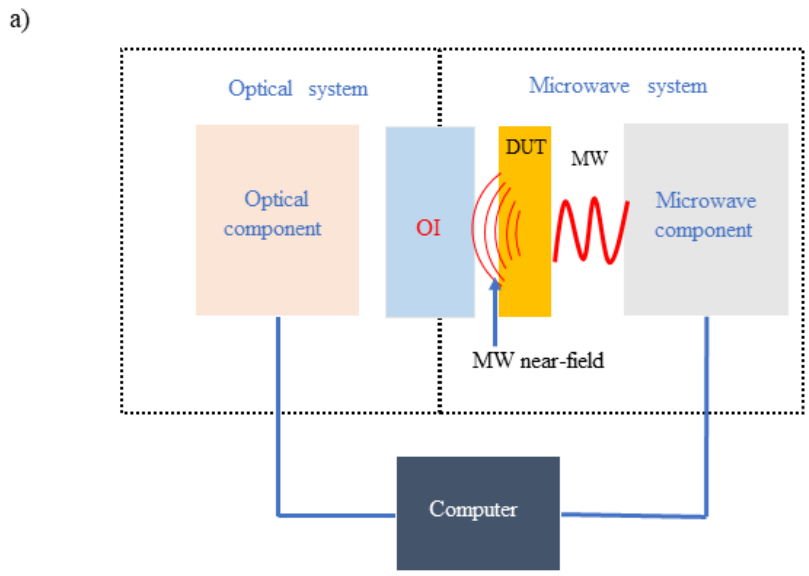

Figure 3.1 Illustration of optical, microwave, and optical indicator sections.

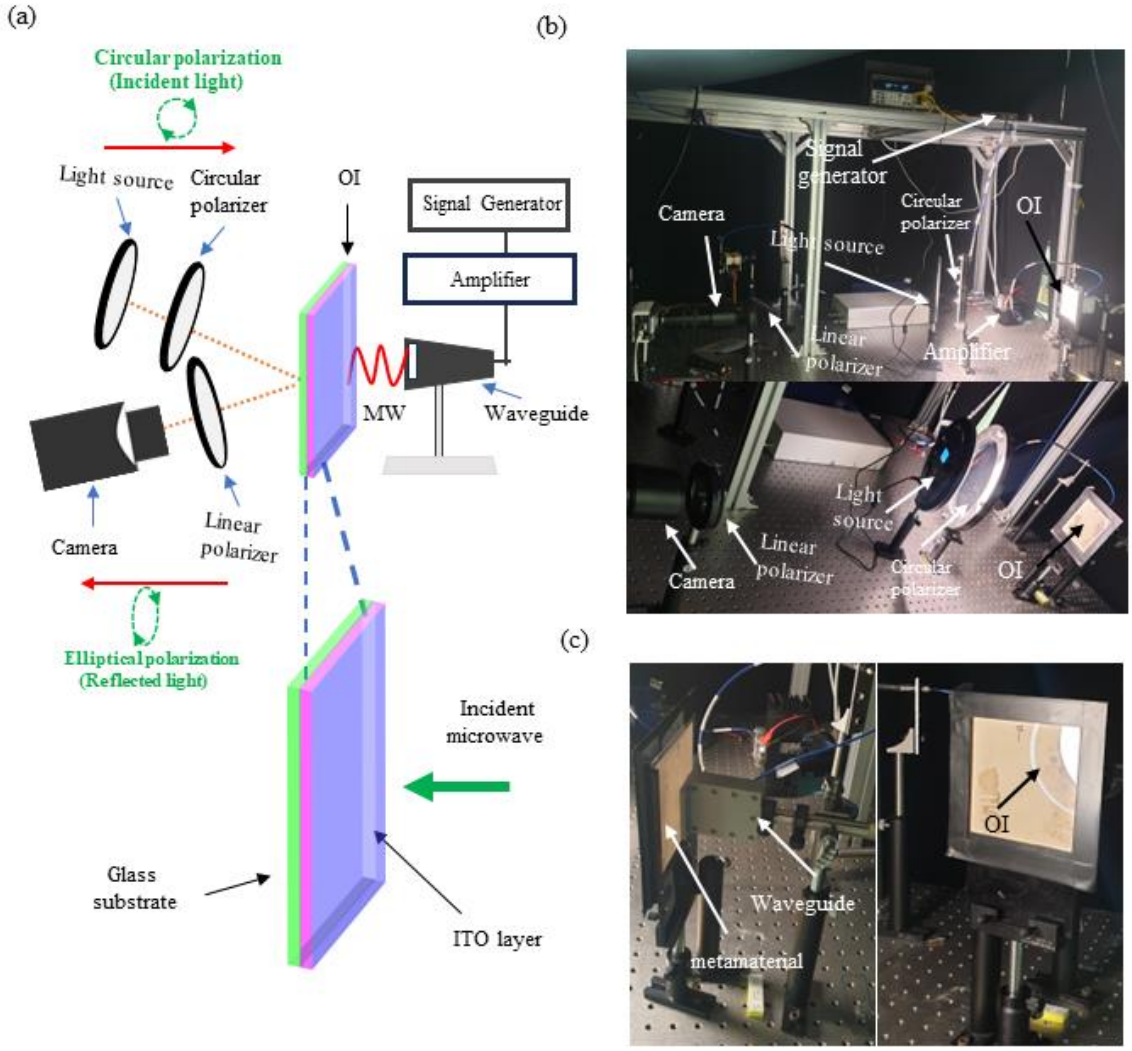

Figure 3.2 (a) An illustration of the measurement setup of TEOIM the magnified part indicates the OI (b) the photos of the measurement setup of TEOM (c) the photos of the front and rear view of the OI.

3.1.1 Microwave Signal Generator and Amplification

An illustration of the experimental setup and photos of the experimental setup is shown in Figure 3.2. In the experiment, a signal generator (Mini-Circuits, SSG-15G-RC) and a signal power amplifier (Mini-Circuits, ZVE-3W-183+) were employed. The initial signal,

generated with a power of -10dBm, was amplified to +34dB before being transmitted through a coaxial cable to a waveguide. X-band TE mode waveguide with internal dimensions of 22.86mm by 10.16 mm was used.

3.2 Optical Polarization and Detection Setup

Light from a light-emitting diode (LED) is circularly polarized after passing through a linear sheet polarizer and a variable full-wave liquid crystal retarder (Thorlab, LCC1423-A). The polarized light illuminates the OI, and the resulting light is reflected and passed through an analyzer. A charge-coupled device (CCD) camera measures the intensity of the light after it passes through the analyzer. The optical indicator (OI) used in this thesis was a glass-coated ITO thin film with dimensions of 10 cm by 10 cm and a thickness of 1 mm, with a film thickness of 200 nm.

3.3 Metamaterial fabrication

3.3.1 Fabrication background

The metamaterial was fabricated at the experimental facilities of the Physics Department of Jeju National University. It was fabricated on an aluminum oxide (Al_2O_3) substrate with dimensions of 100 mm x 100 mm. Using high dielectric constant (ε_r) materials as substrates for resonators offers the advantages of small-sized resonators and improves their performances. High ε_r substrates allow for the miniaturization of resonators by shortening the wavelength of electromagnetic waves within the material, enabling smaller physical dimensions while maintaining the desired resonant frequency. Additionally, high ε_r substrates enhance resonator performance by increasing the quality factor (Q-factor)[1]. The fabrication process involved several steps, including unit cell design, silver pasting, drying, etching, and removal of organic adhesives from the patterned silver solution.

3.3.2 Unit cell design

The foundation of metamaterials lies in the design of the unit cell, a fundamental building block with unique electromagnetic properties. In this thesis, the CST Microwave Studio was utilized to simulate the unit cells [2], [3]. The simulation configuration in the software is depicted in Figure 3.3(a). **Simulation Setup:** In the simulation environment, the unit cell is treated as an infinite periodic structure, employing unit cell boundary conditions along the x and y directions. The structure incorporates an open space (add space) and a perfect electric conductor (PEC) boundary at the front of the metamaterial, as illustrated in Figure 3.3(a).

Unit Cell Structure: The unit cell design is a customized modification of the complementary rectangular split-ring resonator. To tailor the unit cell for a specific frequency range, the outer and inner rectangular rings were connected, and a strip was inserted symmetrically into the inner ring, as illustrated in Figure 3.3(b).

Material Properties: Within the simulation environment, the alumina substrate was specified with a relative permittivity (ε_r) of 9.8. For the metallic pattern, silver metal with an electrical conductivity of 6.3×10^7 S/m was used.

Resonance Properties: To determine the optimal dimensions of the unit cell, the dimensions of the resonator were varied systematically. This process resulted in the identification of the resonant frequency, which was 11.5 GHz.

Key Design Parameters: Based on the simulation and optimization, the primary parameters of the unit cell are detailed in Figure 3.3(c):

- Gap width (g) = 0.1 mm
- Substrate length (h) = 2 mm

- Line width (w) = 0.1 mm
- Length of silver (l) = 1.2 mm
- Thickness of substrate (t) = 1 mm

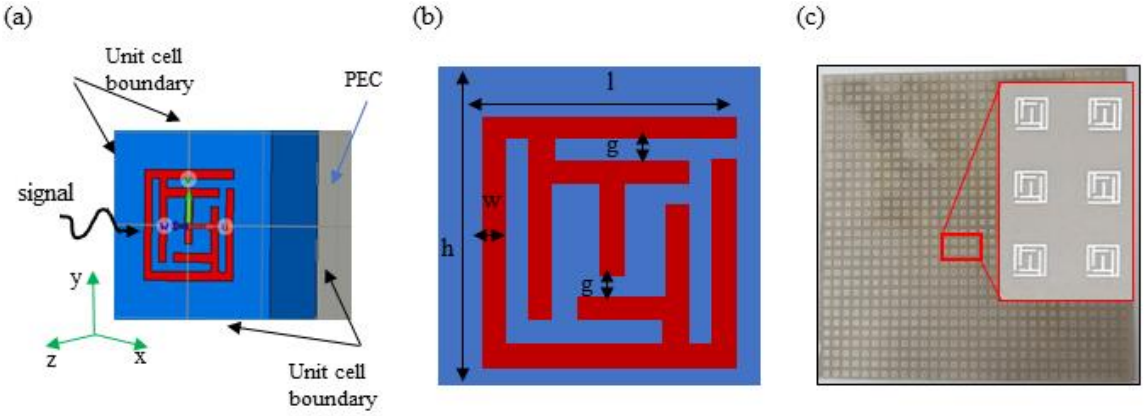

Figure 3.3 Simulation setup (b) Illustration of the unit cell (c) The metamaterial plate and its magnified view.

3.4 Fabrication of metamaterial absorber

Once the design was finalized, the silver paint was applied to the screen using the silver paste technique. A squeegee was used to ensure even distribution by moving it across the surface of the screen. After an even distribution of the silver paint was achieved, the screen was carefully placed on the alumina substrate, and the silver paint was transferred to the substrate. Then, the substrate was dried at 100 degrees Celsius for one hour to remove any moisture. Then, the desired structures were created by laser etching using a JTY FIBER 20 laser machine Figure 3.4 (a). The sample was then subjected to a high-temperature treatment using a furnace (SH-FU-5MG) Figure 3.4 (c) at 800 degrees Celsius for three hours to ensure proper bonding of the silver ink to the substrate and to remove any residual organic solvents. Finally, the sample was gradually cooled to room temperature to avoid thermal shock and ensure the integrity of the fabricated metamaterial.

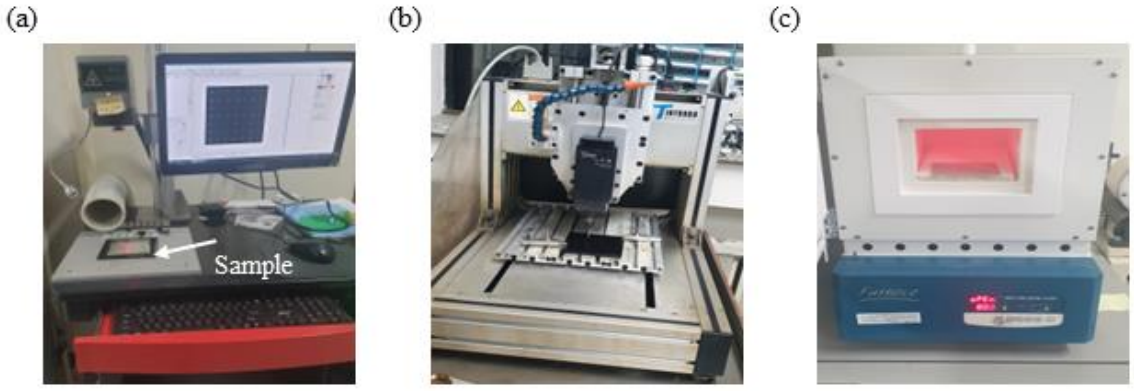

Figure 3.4. (a) JTY FIBER 20 laser machine to design the structure. (b) a computer numerical control (CNC) machine used to create structures on test samples. (c) printing screen. (d) furnace (SH-FU-5MG)

3.5 Thin film fabrication

The thin films were created on a 0.8 mm thick soda-lime glass substrate by depositing aluminum on the surface using a thermal evaporation technique. During the deposition process, the chamber pressure and deposition rate were maintained at 10^{-5} to 10^{-6} Torr and 1 Å/s, respectively. After deposition, the thickness of the aluminum thin films was checked with an optical scanning interferometer. A transmission line was fabricated based on procedure 1.4.

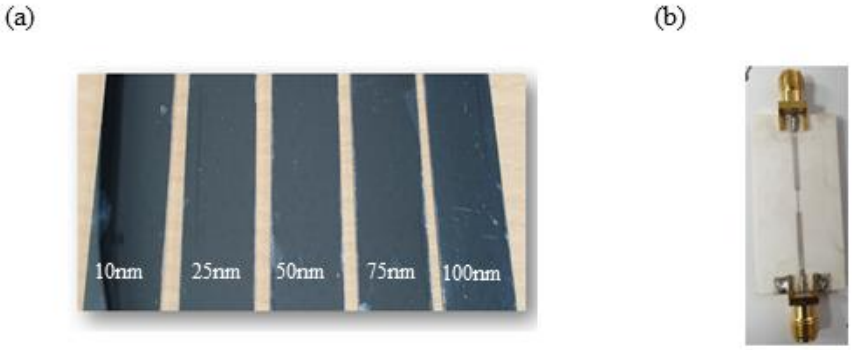

Figure 3.5 (a) images of fabricated aluminum thin films with their respective thickness. (b) photos of the transmission line.

3.6 References.

[1] "Pozar_Microwave Engineering (2012)".

[2] S. A. Mohammed, R. A. Kamil Albadri, and K. S. L. Al-Badri, "Simulation of the microwave five-band a perfect metamaterial absorber for the 5G communication," *Heliyon*, vol. 9, no. 9, Sep. 2023, doi: 10.1016/j.heliyon.2023.e19466.

[3] A. N. Asl, B. Yousif, and M. Al-Zalabani, "Design, modeling, and fabrication of a new compact perfect metamaterial X-band absorber," *AIP Adv*, vol. 10, no. 2, Feb. 2020, doi: 10.1063/1.5143934.

Chapter highlights

This chapter focuses on enhancing sensitivity in thermoelastic optical indicator microscopy (TEOIM) by optimizing thin film thickness. Aluminum thin films with varying thicknesses were fabricated, and the microwave near field was measured for each to investigate their absorption capabilities. The study reveals that thinner aluminum films, particularly with a thickness of 10nm, exhibit higher microwave absorption capability, thus enhancing measurement sensitivity. Thin film thickness is a critical factor in absorption, and therefore, it plays a key role in enhancing TEOIM sensitivity. The findings are further supported by theoretical analysis and calculated microwave absorption.

CHAPTER 4

Thin film optimization for enhanced microwave absorption and measurement sensitivity of TEOIM

4.1 Introduction

Microwave technology plays a pivotal role in nondestructive testing (NDT) methods, allowing us to inspect the integrity and surface conditions of materials and structures without causing any harm [1]– [4]. This technology is of paramount importance in modern industries, leading to extensive research efforts aimed at developing practical NDT techniques [3], [5]–[7]. Among the various methods explored, microwave imaging techniques have gained significant attention due to their cost-effectiveness, remarkable penetration capabilities through dielectric materials, and non-contact measurement capabilities [8]–[12].

One promising approach to microwave-based NDT is Thermoelastic Optical Indicator Microscopy (TEOIM), which offers the advantage of scan-free microwave imaging. TEOIM employs the power of an optical microscopic system equipped with a charge-coupled device (CCD) camera, offering high spatial resolution, a wide field of view, and rapid measurement throughput. This innovative technique has found applications in monitoring electronic devices during operation, characterizing and detecting cracks in conductive thin films, inspecting conductive particles embedded in opaque dielectric materials, non-invasively measuring liquid concentrations, and defect detection in dielectric materials [13]– [18]. However, despite substantial progress in TEOIM applications, one critical aspect has remained unexplored: the enhancement of its measurement sensitivity. The sensitivity of TEOIM crucially depends on the optical indicator ability to convert microwave electromagnetic fields into optical signals.

This chapter aimed to investigate the relationship between the thicknesses of aluminum thin films and microwave magnetic field (H-MWNF) absorption for the improvement of measurement sensitivity of TEOIM. To achieve this, optical indicators with an aluminum thin film of 10nm, 25nm, 50nm, 75nm, and 100nm were prepared, and a microwave transmission line was fabricated as a test sample. When the transmission line was in operation, the H-MWNF was imaged by using the prepared OIs. The result demonstrated a correlation between the thickness of the aluminum thin films and the absorption of the microwave field indicating that the sensitivity of the optical indicator increases as the thickness of the thin films decreases.

4.2 Experiment

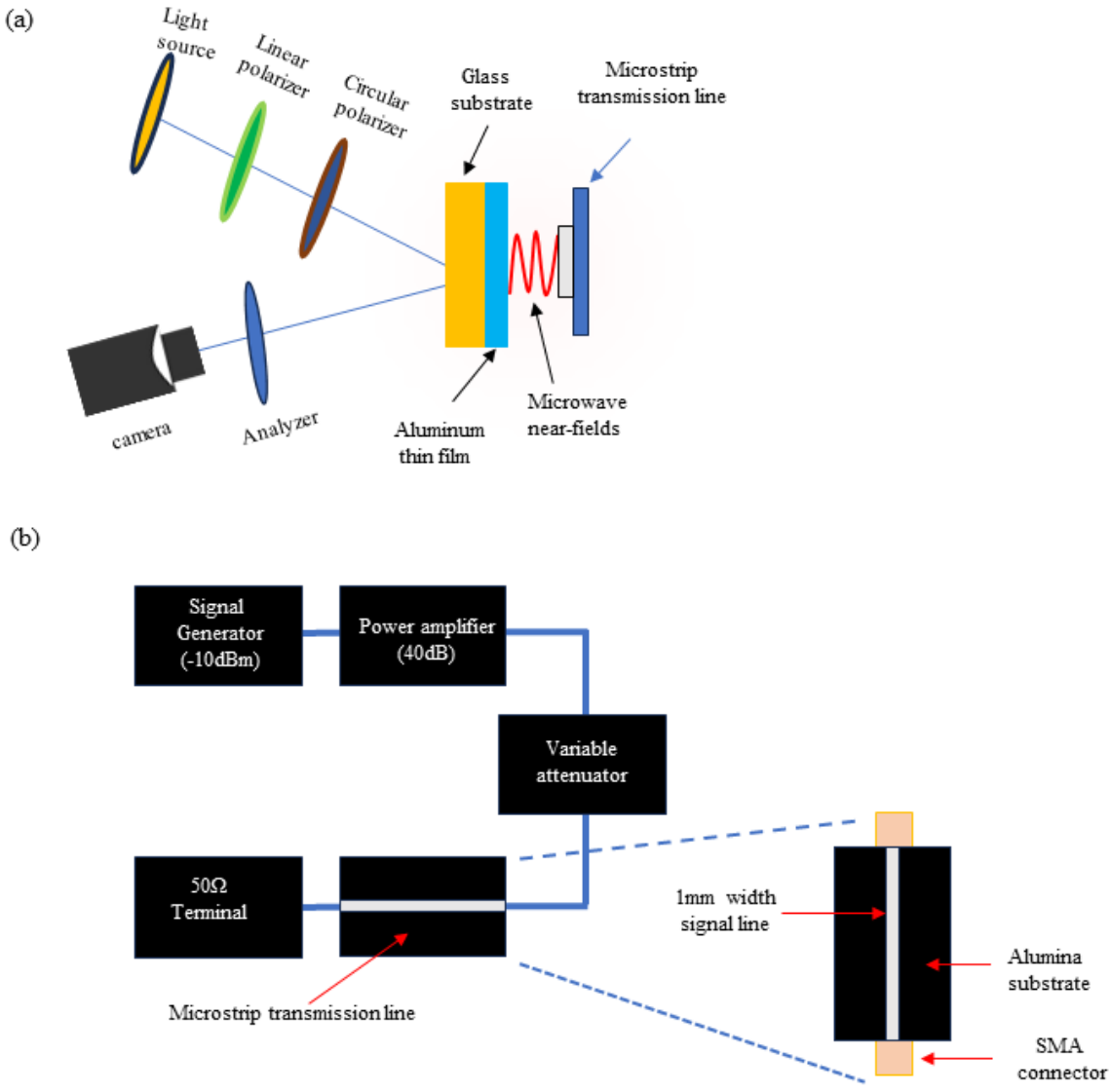

Figure 2.4.1 (a) Measurement setup of the TEOIM. (b) Illustration of the microwave signal generator system.

4.3 Result and discussion

Figure 1(a) shows the experimental setup used to measure the H-MWNF distribution using optical indicators to determine the microwave absorption according to their thickness. The

experimental setup involved the fabrication of a transmission line as a test sample. When the transmission line is operating, it radiates electromagnetic waves in the microwave frequency range. Using the fabricated optical indicators, the H-MWNF distribution was imaged, and their performance is evaluated based on their thickness.

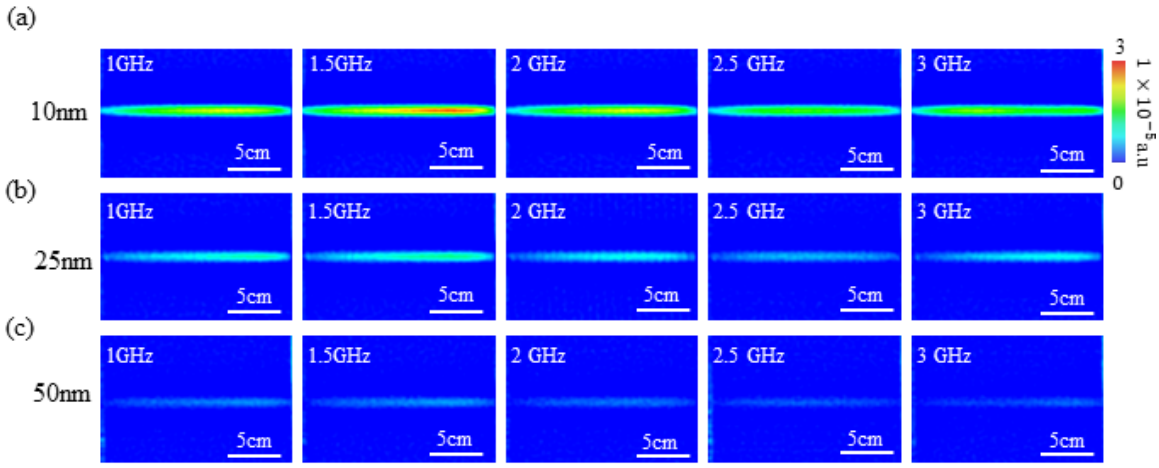

Figure 4.2 The H-MWNF distribution result measured at the frequency range 1GHz to 3GHz for the OIs of 10nm, 25nm, and 50nm.

Figure 4.2 shows the representative results of OIs of 10nm to 100nm. The H-MWNF distribution was measured at frequencies of 1GHz to 3GHz at the input power of 30dBm. The results of this study show that the imaged H-MWNF distribution was found to be consistent with studies in [14]. Additionally, it was observed that the pattern of spatial distribution measurements remained consistent across all optical indicators, regardless of their thickness. This consistency underscores the spatial distribution pattern as an independent parameter in this measurement technique; however, the field intensity was clearly influenced by the thickness of the thin film. A strong field distribution was observed when the thickness of the aluminum thin film was 10nm, indicating that thinner films

possess a higher microwave absorption capability. Conversely, as the thickness of the aluminum thin film increased, the field distribution intensity weakened.

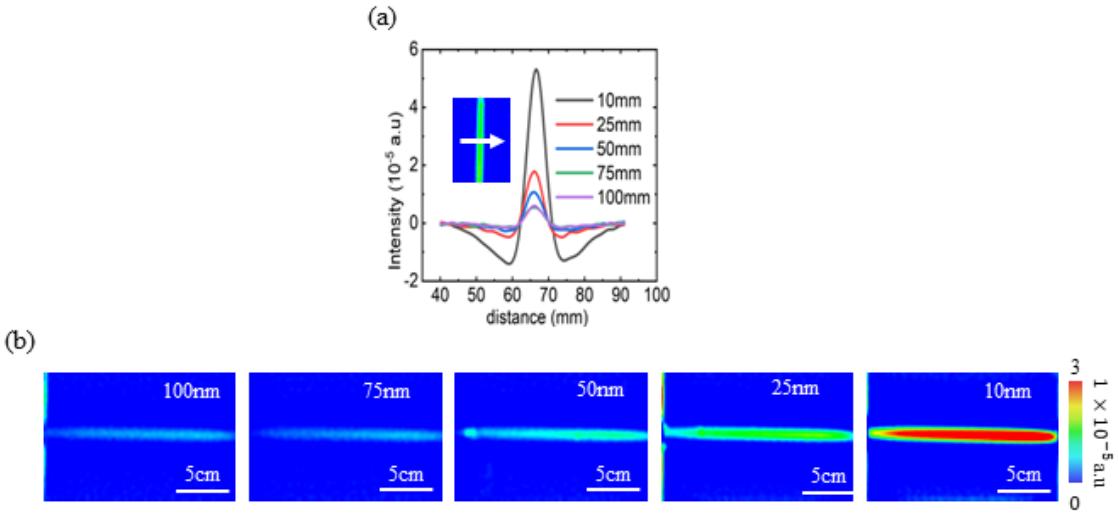

Figure 4.3 (a) Intensity line profile of a microstrip line at 30dBm input power and a frequency of 1.5GHz with optical indicators of 10nm, 25nm, 50nm, 75nm and 100nm respectively. (b) Their corresponding H-MWNF **distribution.**

Figure 4.3 shows the result of the intensity line profile calculated for each optical indicators at resonance frequency of 1.5GHz and the input power of 30dBm. The intensity line profile further confirmed that the intensity of the microwave near field distribution is increased with the reduction of the thin films of the optical indicator. To quantitatively analyze the measurement sensitivity of the optical indicator with respect to the thickness of the aluminum thin film, the intensity of the near field was measured as a function of the microwave input power. Figure 4.4(a) shows the intensity of the microwave near field per microwave input power (I/P) for optical indicators with different thicknesses of aluminum thin films. It shows a fascinating pattern. As the thickness of the aluminum thin film increases from 10nm to 25 nm, the (I/P) intensity decreases rapidly. However, for film

thicknesses greater than 25 nm, the (I/P) value gradually decreased with increasing film thickness.

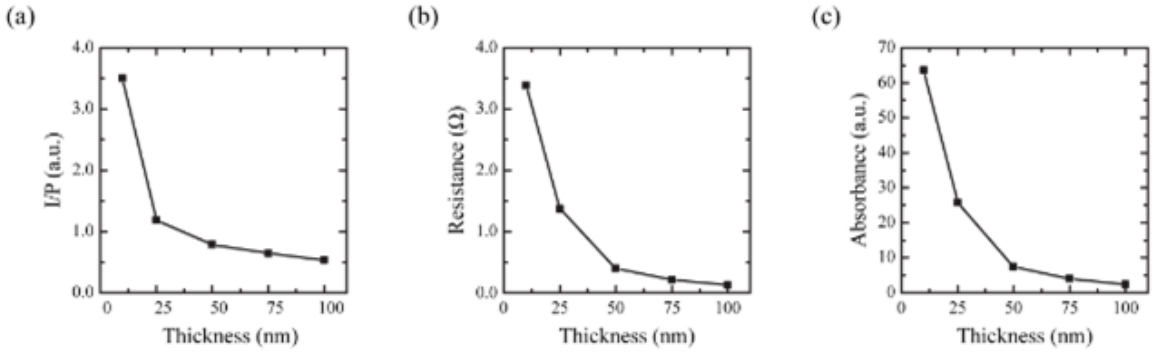

Figure 4.2 (a) Measured near-field intensity per microwave input power (I/P) as a function of the aluminum thin film thickness of the optical indicator. (b) Measured electrical resistance as a function of aluminum film thickness. The electrical resistance was measured by the two-point probe method with 2 mm between the probes. (c) Calculated microwave absorption as a function of aluminum film thickness.

This observation indicates that the measurement sensitivity of the optical indicator is inversely related to the thickness of the aluminum thin film. Thinner films in the range of 10nm to 25 nm exhibit higher (I/P) intensity, indicating greater microwave absorption efficiency. In contrast, the (I/P) intensity decreases for films thicker than 25 nm, suggesting lower microwave absorption efficiency. These results indicate that the sensitivity of microwave field measurement with the optical indicator can be significantly improved when the thickness of the thin film is reduced to 10 nm. The enhanced measurement sensitivity of the optical indicator can be explained by the inverse relationship between the electrical resistance of the metal thin film and the film thickness, as expressed by Equation (4.1).

$$R = \rho \, {}^{L}/_{A} \qquad 4.1$$

In this equation, R represents the electrical resistance of the aluminum thin film, ρ represents its resistivity, while A and L represent the area and length of the aluminum thin film, respectively. The microwave heating of metal thin films is attributed to the electric current induced by the microwave magnetic field, and this heating increases with an increase in the electrical resistance of the thin film. As the electrical resistance of the metal thin film increases with the film thickness, the measurement sensitivity improves as the film thickness decreases. This relationship is further supported by the changes observed in the measured electrical resistance of the aluminum thin film based on the film thickness as shown in Fig. 4.4(b).

Microwave absorption in metal thin films has been investigated in previous studies [19], [20]. To calculate the absorbed microwave power when a metal thin film is used for microwave absorption, the following equation is used.

$$R = \frac{\xi^2}{(1+\xi)^2} \quad , where\ \xi = \frac{L}{s} \tag{4.2}$$

Here A represents the absorbed microwave power, L denotes the thickness of the metal thin film, and s represents the scale length. The scale length s depends on the impedance of the surrounding medium (Z0) and the conductivity of the thin metal film (σ). It can be calculated with the following equation.

$$s = \frac{2}{\sigma Z_0} \tag{4.3}$$

Using equation (4.3), we calculated the absorption of microwave power according to the thickness of the aluminum thin film, as shown in Figure 4.4(c). In this calculation, the conductivity of the aluminum was assumed to be 3.5×10^7 S/m and Z0 was assumed to be

377 Ω. The calculated microwave absorption showed a behavior consistent with the sensitivity of the indicator with respect to the thickness of the aluminum thin film. It can be concluded that the increase in the sensitivity of the microwave magnetic field in the optical indicator is due to the increase in the electrical resistance as the thickness of the aluminum thin film decreases, which in turn enhances the microwave heating.

4.4 Conclusion

In summary, the study focused on enhancing the H-MWNF absorption of thin films of the optical indicator for the improvement of the microwave field measurement sensitivity of TEOIM. OIs with thin film thickness ranging from 10nm to 100nm were prepared, and their corresponding H-MWNF distribution was measured from the test sample of the microstrip transmission line. The investigation examined the correlation between film thickness and microwave field absorption. The findings confirm the pivotal role of film thickness in microwave absorption enhancement, with the 10nm thin film demonstrating enhanced performance compared to other samples. The enhanced microwave absorption of the optical indicator has improved the measurement sensitivity of TEOIM. Theoretical analysis indicates that reducing the thickness of the aluminum thin film increases resistance, subsequently enhancing microwave heating efficiency, and, in turn, improving the measurement sensitivity of the optical indicator. In conclusion, the thickness of the metal thin film in the optical indicator stands as a critical factor in enhancing microwave absorption and improving the microwave measurement sensitivity in TEOIM.

4.5 Reference

[1] H. Zhang, R. Yang, Y. He, A. Foudazi, L. Cheng, and G. Tian, "A review of microwave thermography nondestructive testing and evaluation," *Sensors (Switzerland)*, vol. 17, no. 5. MDPI AG, May 15, 2017. doi: 10.3390/s17051123.

[2] W. S. Teng, M. Firdaus Akbar, G. Nihad Jawad, S. Y. Tan, and M. I. S. Mohd Sazali, "A past, present, and prospective review on microwave nondestructive evaluation of composite coatings," *Coatings*, vol. 11, no. 8. MDPI AG, Aug. 01, 2021. doi: 10.3390/coatings11080913.

[3] W. Nsengiyumva, S. Zhong, J. Lin, Q. Zhang, J. Zhong, and Y. Huang, "Advances, limitations and prospects of nondestructive testing and evaluation of thick composites and sandwich structures: A state-of-the-art review," *Composite Structures*, vol. 256. Elsevier Ltd, Jan. 15, 2021. doi: 10.1016/j.compstruct.2020.112951.

[4] B. Wang, S. Zhong, T. L. Lee, K. S. Fancey, and J. Mi, "Non-destructive testing and evaluation of composite materials/structures: A state-of-the-art review," *Advances in Mechanical Engineering*, vol. 12, no. 4. SAGE Publications Inc., Apr. 01, 2020. doi: 10.1177/1687814020913761.

[5] H. Thomas, "TechSolutions 1: A Brief Introduction to Nondestructive Testing." [Online]. Available: http://ammtiac.alionscience.com

[7] H. Zhang, R. Yang, Y. He, A. Foudazi, L. Cheng, and G. Tian, "A review of microwave thermography nondestructive testing and evaluation," *Sensors (Switzerland)*, vol. 17, no. 5. MDPI AG, May 15, 2017. doi: 10.3390/s17051123.

[8] H. S. El-Mesery, H. Mao, and A. E. F. Abomohra, "Applications of non-destructive technologies for agricultural and food products quality inspection," *Sensors (Switzerland)*, vol. 19, no. 4. MDPI AG, Feb. 02, 2019. doi: 10.3390/s19040846.

[9] "IEEE Instrumentation & Measurement Magazine," 2007.

[10] “N. Qaddoumi et al.: Detecting Defects in Outdoor Non-ceramic Insulators using Near-field Microwave Non-destructive Testing,” 2010.

[11] H. Xu, T. Li, and Y. Sun, “The Application Research of Microwave Imaging in Nondestructive Testing of Concrete Wall *.”

[12] M. Benedetti, M. Donelli, A. Martini, M. Pastorino, A. Rosani, and A. Massa, “An innovative microwave-imaging technique for nondestructive evaluation: Applications to civil structures monitoring and biological bodies inspection,” *IEEE Trans Instrum Meas*, vol. 55, no. 6, pp. 1878–1883, Dec. 2006, doi: 10.1109/TIM.2006.884287.

[13] H. Lee, Z. Baghdasaryan, B. Friedman, and K. Lee, “Detection of a Conductive Object Embedded in an Optically Opaque Dielectric Medium by the Thermo-Elastic Optical Indicator Microscopy,” *IEEE Access*, vol. 7, pp. 46084–46091, 2019, doi: 10.1109/ACCESS.2019.2908885.

[14] H. Lee, S. Arakelyan, B. Friedman, and K. Lee, “Temperature and microwave near field imaging by thermo-elastic optical indicator microscopy,” *Sci Rep*, vol. 6, Dec. 2016, doi: 10.1038/srep39696.

[15] S. Hamelo, J. Yang, and H. Lee, “Detection of Defects in a Dielectric Material by Thermo-Elastic Optical Indicator Microscopy,” *IEEE Access*, vol. 11, pp. 45961–45971, 2023, doi: 10.1109/ACCESS.2023.3274534.

[16] H. Lee, “Detection of Air Bubbles and Liquid Droplet in a Dielectric Tube by Thermo-Elastic Optical Indicator Microscopy,” *IEEE Access*, vol. 10, pp. 33537–33546, 2022, doi: 10.1109/ACCESS.2022.3162247.

[17] S. Arakelyan, H. Lee, Y. Jeong, A. Babajanyan, B. Friedman, and K. Lee, “Direct imaging of the SSD and USB memory drives heating by thermo-elastic optical indicator microscopy,” *Case Studies in Thermal Engineering*, vol. 10, pp. 407–412, Sep. 2017, doi: 10.1016/j.csite.2017.09.008.

[18] Z. Baghdasaryan, A. Babajanyan, L. Odabashyan, H. Lee, B. Friedman, and K. Lee, “Visualization of Microwave Heatingformesh-Patterned Indium-tin-Oxide by a Thermo-Elastic Optical Indicator Microscope,” 2018.

[19] H. Bosman, Y. Y. Lau, and R. M. Gilgenbach, “Microwave absorption on a thin film,” *Appl Phys Lett*, vol. 82, no. 9, pp. 1353–1355, Mar. 2003, doi: 10.1063/1.1556969.

[20] H. Sueyoshi and S. Kakiuchi, “Microwave heating of thin Au film,” *Mater Trans*, vol. 48, no. 3, pp. 531–537, Mar. 2007, doi: 10.2320/matertrans.48.531.

Chapter highlights

In this chapter, the integration of metamaterial absorbers with optical indicator to improve microwave absorption and sensitivity in microwave H-MWNF measurements is investigated. The experimental setup, design, and fabrication of metamaterials, as well as the measurement principles are presented. The result shows a tenfold increase in measurement sensitivity with integrated metamaterials, demonstrating improved absorptivity.

CHAPTER 5

Metamaterial integration for enhanced microwave absorption of the optical indicator and measurement sensitivity of TEOIM

5.1 Introduction

Microwave absorbing materials, with their ability to convert electromagnetic energy into heat serve as essential components in various technological applications [1]– [6]. Among these materials, thin films have emerged as remarkable candidates for their efficiency in absorbing electromagnetic waves [7]– [12]. This unique property finds a compelling application in Thermoelastic Optical Indicator Microscopy (TOIM)**.** It is a new technique to visualize the microwave near field distribution that relies on the microwave absorption of thin films coated on the glass substrate as an optical indicator[13]. TEOIM enables the visualization and measurement of microwave near-field distribution with remarkable sensitivity[13], [14]. Its measurement sensitivity depends on the microwave absorption efficiency of a thin film within the optical indicator [13]. Therefore, increasing the absorption efficiency of the thin film of the optical indicator improves the measurement sensitivity of TEOIM.

Various strategies have been explored to enhance the microwave absorption of thin films intended for optical indicator applications. One approach involves the use of aluminum nanoparticles (AlNP) coated with a poly (methyl methacrylate) (PMMA) thin film, which has been utilized for imaging the microwave electrical component due to its high microwave absorption [13], [15]. Another technique includes the incorporation of good conductors such as platinum, indium tin oxide (ITO), and aluminum metal thin films, contributing to increased absorption of the magnetic microwave component [16]– [21].

Recently, metal thin films integrated with metamaterial absorbers (MM-ABS) have shown promising results in improving the microwave absorption of thin films [22]– [28]. MM-ABS consists of subwavelength structures smaller than the wavelength of the incident waves, allowing them to interact with the waves in unique ways [29]– [32]. By independently manipulating the dimensions of the resonant component within the unit cell, the MM-ABS can achieve an impedance match to free space. This leads the absorber to minimize wave transmission and reflection and effectively maximizes absorption [33], [34]. The ability to control and manipulate electromagnetic waves at this scale offers significant advantages in improving microwave absorption. This method has advantages such as cost-effectiveness and ease of fabrication, flexibility in design, tunability of absorption characteristics, and ease of integration into existing microwave devices and systems [35].

In this work, metamaterial absorbers (MM-ABS) were integrated with the optical indicator (OI) to enhance its microwave absorption without altering the optical indicator. The optical indicator investigated was an indium thin oxide (ITO) film deposited on a glass substrate. The MM-ABS consists of 36x36 resonators operating at a frequency of 11.5 GHz and was fabricated on an alumina substrate. Silver metal was used to manufacture resonators. The backside of the MM-ABS was intentionally not coated with metal to facilitate integration with the ITO layer of the optical indicator. This integration ensures as MM-ABS is grounded with a conductive ITO layer. When the MM-ABS is at the resonant frequency, the ITO layer exhibits strong absorption, which enables efficient microwave signal transmission between the MM-ABS and the ITO layer of the OI. Microwave near-field measurements were performed with and without MM-ABS to evaluate the microwave absorption. The results show that the intensity of the microwave near-field increases in the presence of the MM-ABS, indicating improved microwave absorption. The calculated sensitivity at the maximum absorption frequency showed 10 times increase compared to the configuration without MM-ABS integration.

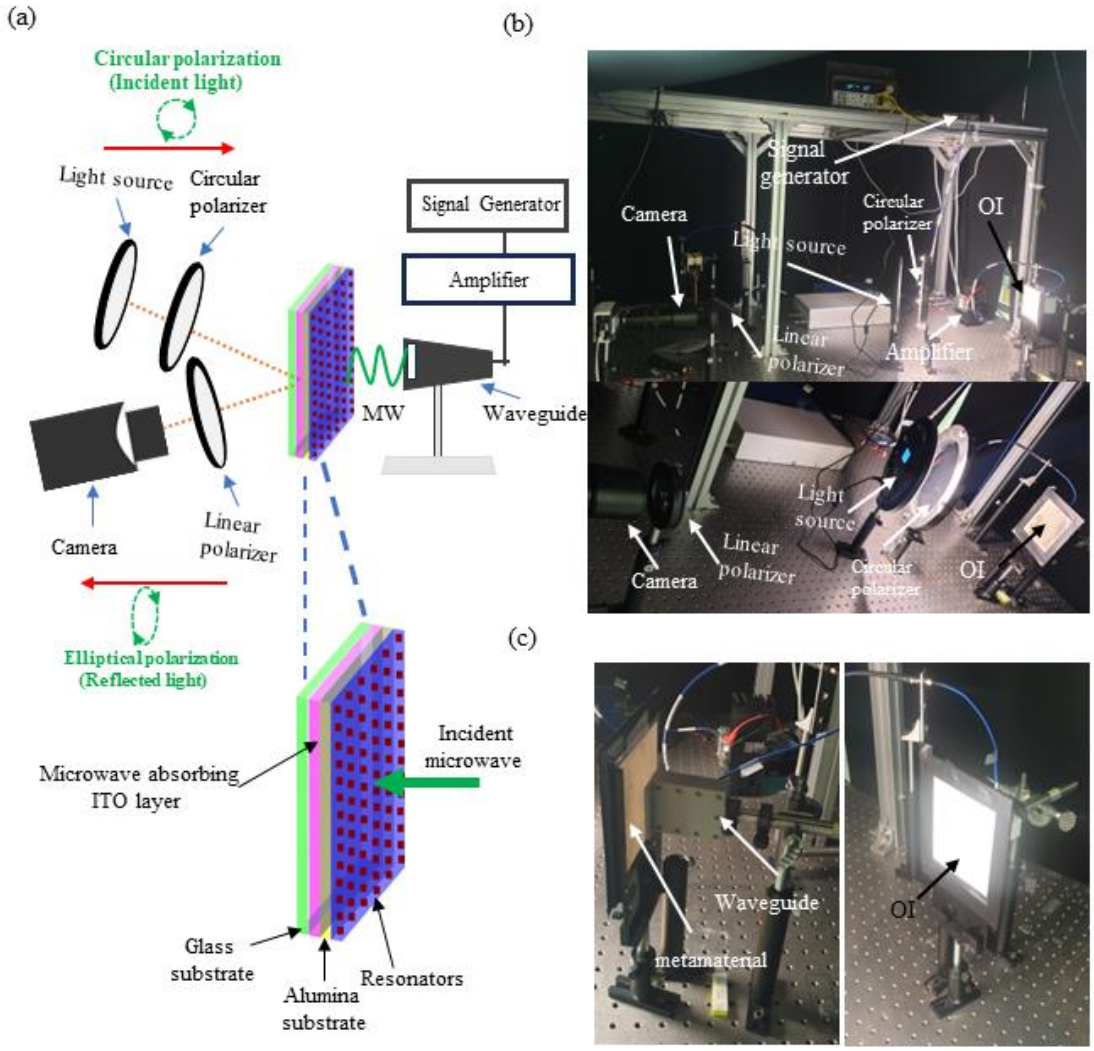

Figure 5.1. (a) Illustrates the measurement setup and the enlarged portion in the illustration that shows the configuration of the metamaterial with the optical indicator (b) photos of the measurement setup. (c) the front and rear views of OI.

5.2 Experiment

5.3 Design, simulation, and fabrication of metamaterial absorber.

The simulation experiments were conducted using the CST Microwave Studio Suite, 2019. Figure 5.2(a) shows the simulation setup in the software. The unit cell is simulated in an

infinite periodic structure with unit cell boundary conditions along the x and y directions, an open space, and a PEC at the front of the metamaterial. Figure 6.2 (b) illustrates the structure of the unit cell, which is a modification of the complementary rectangular split ring resonator. This modification involves connecting the outer and inner rectangular rings and symmetrically inserting a strip into the inner ring to achieve the small dimensions of the unit cell for the required frequency range.

In the simulation environment, an alumina substrate (εr = 9.8) and silver were used for the metal pattern, with a conductivity of 6.3× 107 S/m. Systematically varying the dimensions of the resonator allowed the observation of resonance characteristics. The dimensions were successfully determined through optimization, resulting in a resonance frequency of 11.56 GHz. The main parameters of the structure, including gap width (g), substrate length (h), line width (w), length of structure (l), and thickness of substrate (t), are presented in the following figure: g = 0.1mm, h = 2mm, w = 0.1mm, l = 1.2mm, and t = 1mm.

Upon completion of the unit cell structure design, the metamaterial was printed on a 100 mm x 100 mm alumina substrate. The printing process was carried out using a laser machine (JTY Fiber 20) after applying silver paste in the first step. Then, the printed structure went through a 3-hour drying process in the furnace (SH-FU-5MG) at a temperature of 800 degrees Celsius to ensure strong adhesion between the metal structure and the substrate. The fabricated metamaterial plate is presented in Figure 6.1 (c).

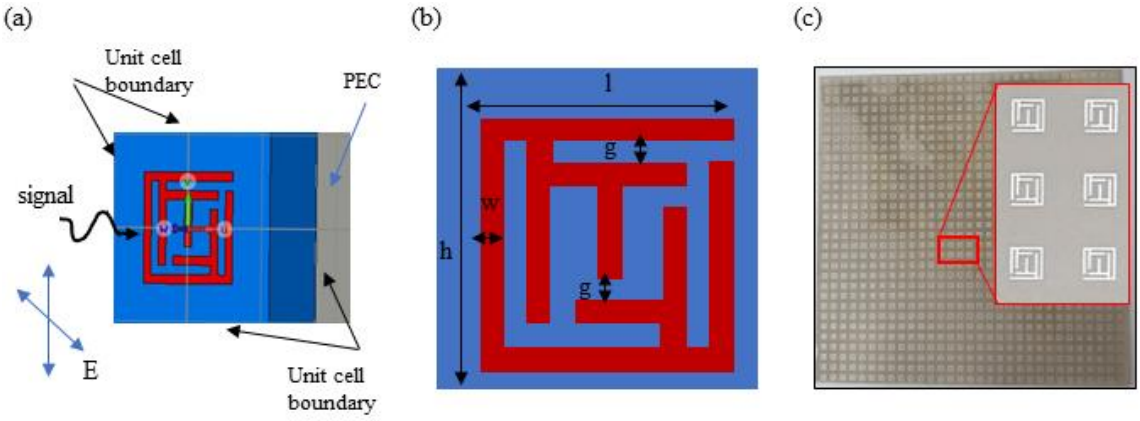

Figure 5.2.simulations setups, unit cell structure and metamaterial plate. **Figure 2 (a) Simulation setup (b) Illustration of the unit cell (c) The metamaterial plate and its magnified view of its unit cell.**

5.3.1 Experimental setup and working principle.

Figure 5.1 (a), illustrates the experimental setup for Thermoelastic Optical Indicator Microscopy (TEOIM) to measure the microwave near-field distribution with MM-ABS. The magnified view within Figure 5.1 (a) illustrates the specific configuration of the metamaterial with the Optical Indicator (OI). The OI, in this experiment, consists of a glass substrate coated with an Indium Thin Oxide (ITO). When the MM-ABS is placed onto the ITO layer of the optical indicator, the configuration is established as a perfect metamaterial absorber grounded by the ITO metal layer.

The working principle of MM-ABS integration with the OI to improve microwave absorption is based on the resonance properties of the MM-ABS and the absorption properties of the ITO thin film. When the MM-ABS is at the resonant frequency, the resonators are coupled to the incident microwaves and achieve impedance matching with free space [29]. This property results in minimum reflection at the interface; therefore, many signals can be absorbed within the MM-ABS. Unlike the metamaterial perfect absorber

configuration, where a metal ground is used to eliminate transmission, in this configuration, the transmitted signals are absorbed by the ITO thin film layer of the OI. The heat induced due to the absorption of the OI is diffused to the glass substrate and measured as an optical intensity based on the measurement principle of the TEOIM [13].

Since the ITO is a conductive material, the microwave magnetic field is absorbed and converted into heat due to the resistive loss of the ITO layer. Therefore, the field intensities measured in this method are the microwave magnetic fields (H-MWNF).

5.4 Result and Discussion.

To investigate the microwave absorption enhancement of the optical indicator by integrating the metamaterial absorber (MM-ABS), The microwave near-field (H-MWNF) distribution was measured using the measurement setup shown in Figure 5.1(a). The measurement was performed in the frequency range of 8GHz to 14GHz.

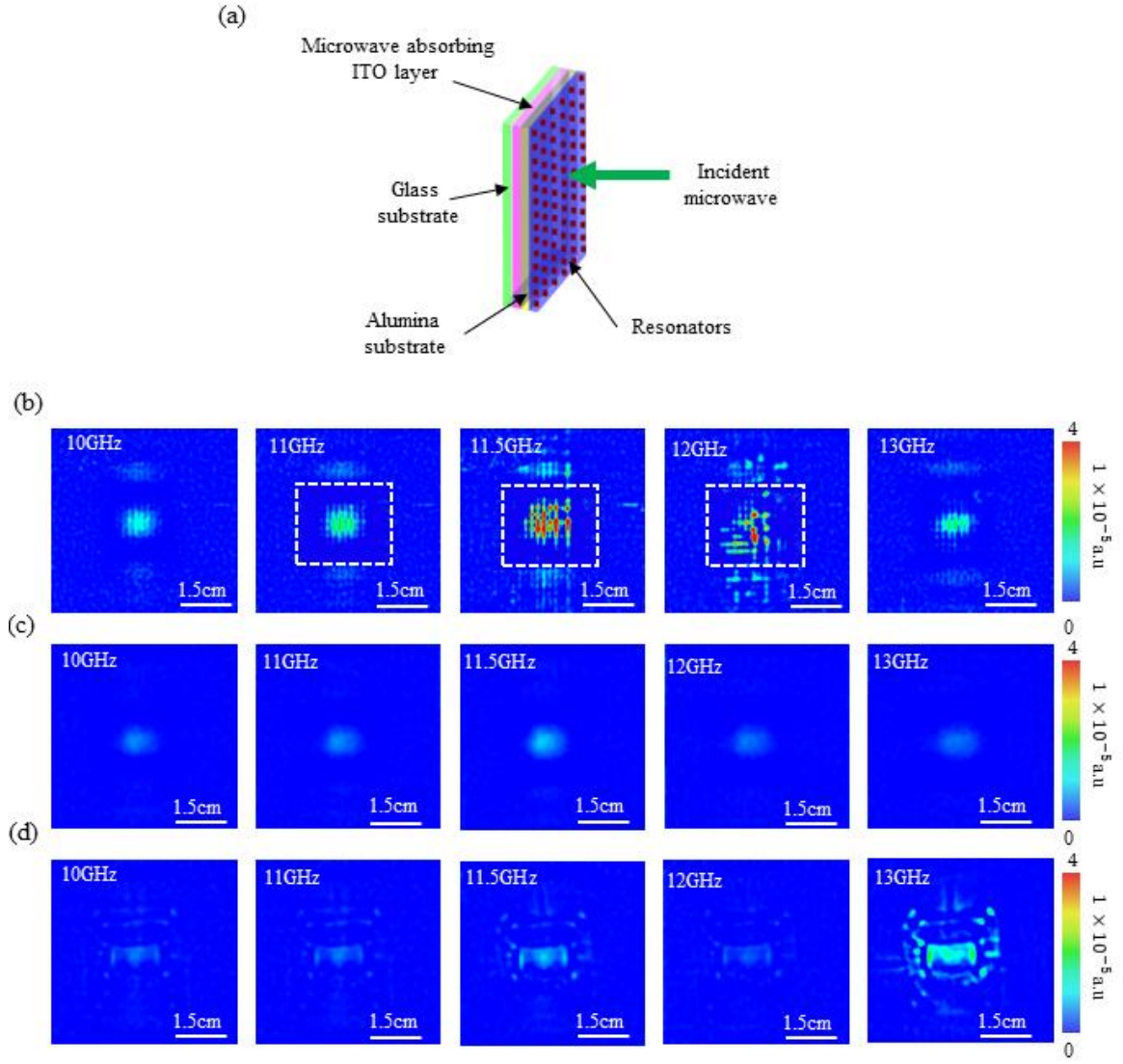

Figure 5.3. shows the result of the measured H-MWNF distributions of the three measurements from the frequencies of 10GHz to 13GHz. (a) the measurement configuration (b) with MM-ABS. (c) With alumina substrate. (d) optical indicator only.

Three different measurements were performed to evaluate the absorption enhancement. The OI and MM-ABS configuration was based on figure 5.3 (a). The first measurement involved placing an optical indicator with a substrate of MM-ABS (alumina) alone, which served as the baseline for comparison. In the second measurement, the MM-ABS was integrated with the OI, while the third configuration involved the optical indicator alone, representing the absence of the MM-ABS. Based on these experiments, Figure 5. 3 (b) shows the results of

the H-MWNF distribution with MM-ABS, while Figure 3 (c) shows the results of H-MWNF distribution with the alumina substrate, and Figure (d) shows the results of microwave H-MWNF distributions without MM-ABS. The result shows that strong H-MWNF intensity is observed at the frequency of 11.5GHz when the OI is integrated with the MM-ABS compared to the two measurements. This indicates that the presence of the metamaterial in the measurement configuration enhanced the H-MWNF intensity at 11.5 GHz.

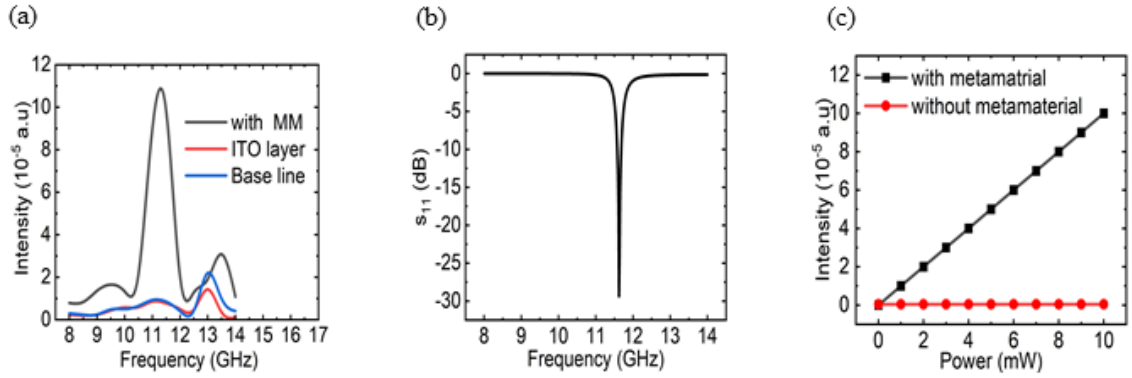

Figure 5.4. (a) H-MWNF intensity as a function of frequency measured with metamaterial (black) with substrate only (red) and optical indicator only (blue). (b) Reflection coefficient from the simulation (c) the calculated intensity changes as a function of power at the frequency of 11.5GHz with MM-ABS and without MM-ABS.

Figure 5.4 (a) shows the calculated H-MWNF intensity as a function of the frequency. The microwave H-MWNF intensity calculation was performed for the three measurements in similar regions, the rectangular region shown in Figure 5.3 (b). Based on this, the pick intensity is observed at the frequency of 11.5 GHz, and the intensity is dropped outside these frequencies.

The peak intensity observed in this result further confirms the enhanced microwave absorption of the OI at the resonant frequency of the MM-ABS. Figure 5.4 (b) show the simulation results of the reflection coefficient. The simulation results show that the reflection coefficient exhibits a minimum reflection at the specific frequency of 11.5 GHz. Indicating

that the resonators are efficient in transferring microwaves at the air MM-ABS interface at this frequency. This demonstrates that the metamaterial minimized wave reflection and maximized absorption in the ITO layer of the OI. This, in turn, contributes to the enhanced sensitivity of TEOIM for measuring H-MWNF distribution.

To quantify the improvement in sensitivity resulting from the increased absorption of the OI, an analysis of the intensity changes as a function of incident microwave power at the resonant frequency of 11.5 GHz was performed based on equation 5.1 [13].

$$S = {}^{\Delta I}/_{\Delta P} \qquad 5.1$$

Here, ΔS represents the sensitivity, ΔI represents the change in near-field intensity, and ΔP represents the change in input power. Figure 5.4(c) shows calculated result of the change in output intensity as a function of input power. The result shows that the intensity increases linearly with the increase in incident microwave power. This linear relationship is consistent with other studies in [13]. However, the configuration with MM-ABS has a significantly higher sensitivity than the configuration without MM-ABS. More precisely, a 10 times improvement was observed. At the resonant frequency of 11.5 GHz, the metamaterial efficiently absorbs microwave signals and transfers them to ITO layer of the optical indicator. This results in increased sensitivity, allowing the measurement system to better detect and respond to changes in incident microwave power.

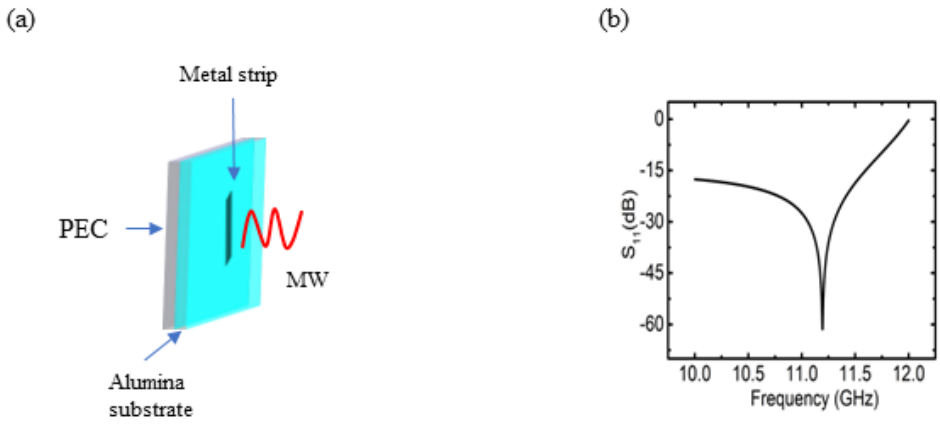

Figure 5.5. (a) Measurement setup for testing the metal strip in the simulation environment (b) the simulated reflection coefficient of the metal strip.

To evaluate the sensitivity enhanced, the experiment was performed with MM-ABS and without MM-ABS by fabricating a silver metal strip on the alumina substrate. The dimensions of the metal strips are 1 mm in width and 4 mm in height, while the dimensions of the substrate are 40 x 20 mm. Before performing the experiment, the response of the metal strip was simulated using CST microwave studio based on the configuration in Figure 5.5 (a). The reflection coefficient of the metal strip showed a resonant frequency of 11.2 GHz. Based on this, the two configurations were evaluated by placing the metal strip between the waveguide and the configuration with MM-ABS and without MM-ABS.

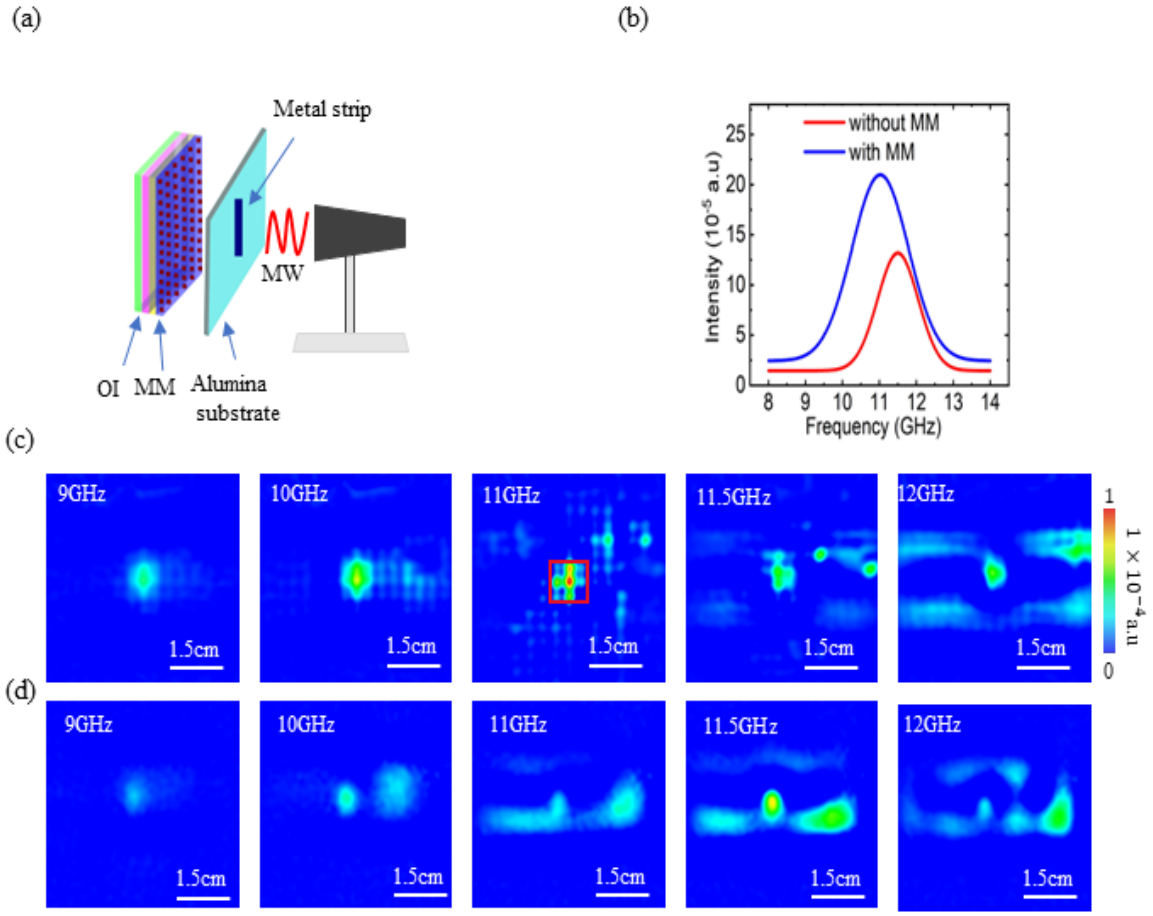

Figure 5.6. Measurement setup for testing the metal strip (b) Calculated H-MWNF as a function of frequency (c) The H-MWNF with metamaterial (d) The H-MWNF distribution without metamaterial.

The fabricated strip was placed at 4 mm from the two configurations as shown in Figure 5.6 (a) and the H-MWNF distribution was measured in the two configurations. Figure 5.6 (b) shows the intensity as a function of frequency. Figure 5.6 (c) and (d) shows the H-MWNF distribution with MM-ABS and without MM-ABS respectively.

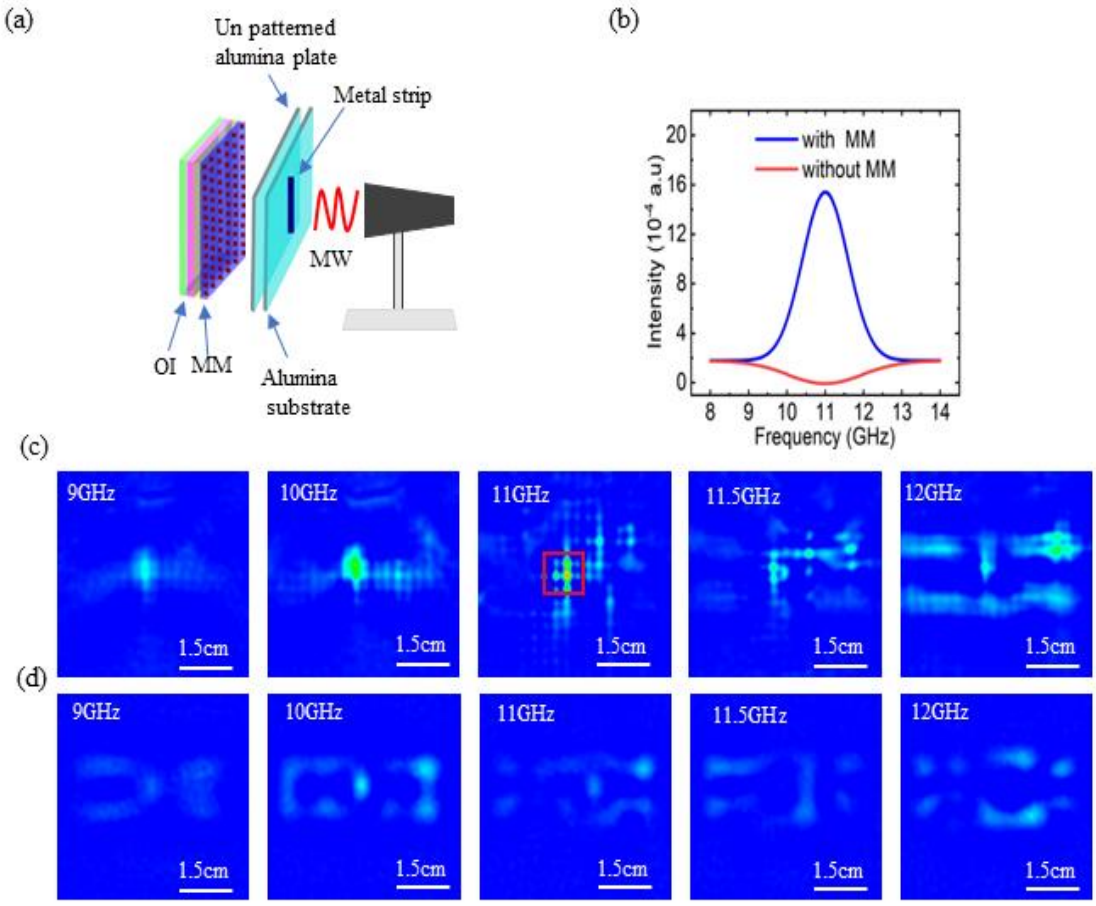

Figure 5.7 . (a) Measurement setup for testing the metal strip (b) Calculated H-MWNF **as a function of frequency (c) The** H-MWNF **distribution with metamaterial (d) The** H-MWNF **without metamaterial.**

The result shows a strong H-MWNF distribution at 11 GHz for the configuration with MM-ABS and a strong field distribution at 11.5GHz for the configuration without MM-ABS. However, the intensity line profile shows that the configuration with MM-ABS has higher intensity than without MM-ABS shown in Figure 5.6 (b). The small resonance frequency shift difference observed in MM-ABS integrated measurement may rise due to the coupling between the metamaterial resonator and the metal strip.

In the previous measurement setup, both configurations, one with MM-ABS and the other without MM-ABS, demonstrated their capability to detect the presence of the metal strip.

However, to further evaluate and determine their performance, a non-patterned alumina plate was placed at the back of the previous experiment as shown in Figure 5.7(a). The purpose of this setup was to deliberately reduce the field intensity that could be detected by both configurations. Based on these Figure 5.7 (b) shows the intensity as a function of frequency. Figure 5.7 (c) and (d) shows the measured H-MWNF distribution with MM-ABS and without MM-ABS. The results obtained from this experiment showed that the MM-ABS integrated configuration remains effective in detecting the metal strip, reaffirming its capability and sensitive measurements. The configuration without metamaterial could not detect the metal strip under the reduced field intensity conditions. It further emphasizes the significant role played by MM-ABS in enhancing the ability of the system to detect and respond to microwave signals efficiently.

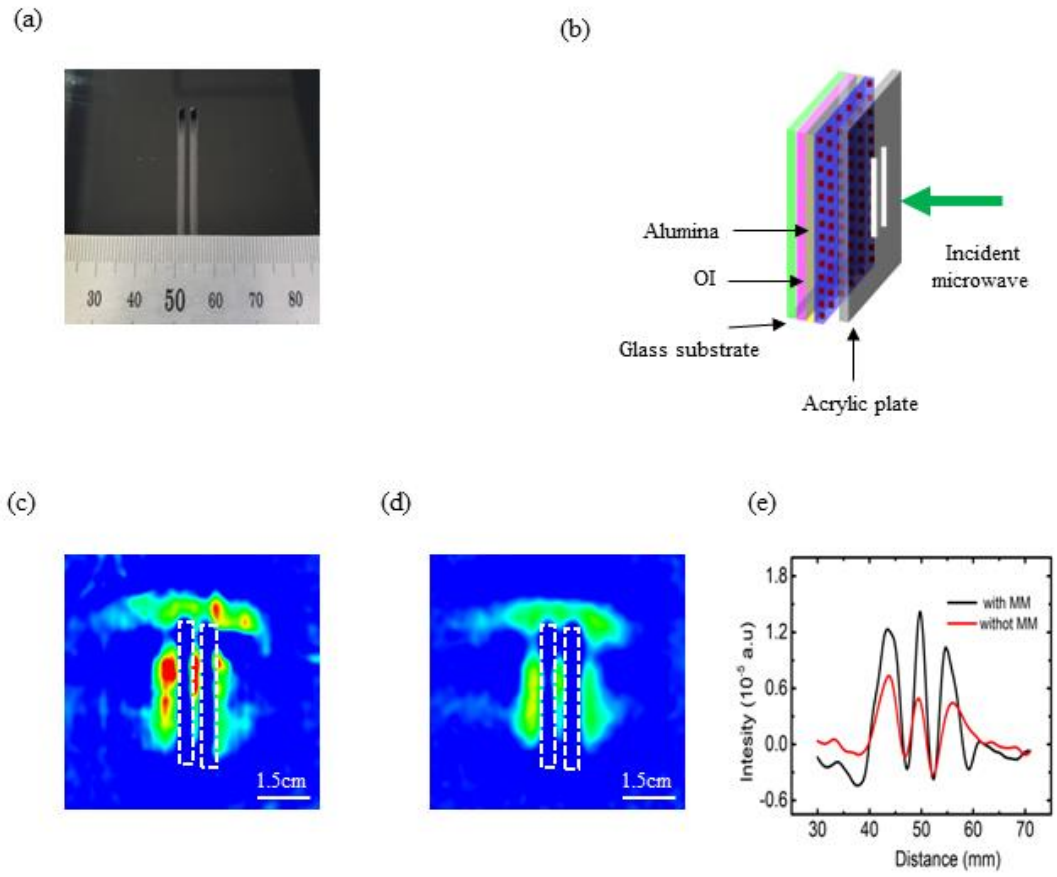

Figure 5.8. (a) Measurement setup for testing the acrylic plate (b) image of the test sample (c) The intensity line profile of the test sample with MM-ABS and without MM-ABS (d) the microwave near field distribution imaged with MM-ABS (e) the H-MWNF **distribution measured without MM-ABS**

The intensity line profile analysis reinforces these observations. In the configuration without metamaterial, the intensity line profile does not exhibit any evidence of the existence of a metal strip. The experiment involving the covered metal strip provides compelling evidence of the pivotal role of the metamaterial in enhancing the sensitivity and performance of the configuration. Even in conditions of reduced field intensity deliberately introduced by the alumina plate, the configuration with metamaterial remains effective in detecting the metal strip. This result is of particular significance for applications where the detection of weak microwave signals is essential.

Finally, an additional test sample with dimensions of 100mm by 100mm and two rectangular slots on it, each measuring 1mm in width and 20mm in height is prepared on the acrylic plate as shown in Figure 5.8 (a), the H-MWNF distribution was measured based on the configuration shown in Figure 5.8 (b). Figure 5.8 (c) shows the results of measured H-MWNF and Figure 5.8 (d) shows the intensity line profile measured across the slots. In both configurations the existence of two slots were detected. However, the measurement result with MM-ABS showed high intensity.

This implies that metamaterial integration enables more detailed measurements of H-MWNF distributions. The measurement with this additional experiment validates the effectiveness of MM-ABS integration in enhancing the sensitivity of H-MWNF measurements and its effectivity in non-destructive defect detection applications.

5.5 Conclusion

In summary, this chapter successfully demonstrated the integration of metamaterial absorbers (MM-ABS) with optical indicators to enhance microwave absorption and improve the measurement sensitivity of thermoelastic optical indicator microscopy (TEOIM). The MM-ABS was designed to operate at 11.5 GHz and was integrated with the optical indicator (OI), and microwave near-field (H-MWNF) distribution measurements were conducted under both MM-ABS-integrated and non-integrated conditions.

The integration of MM-ABS resulted in a large improvement in microwave absorption within the OI, consequently leading to a remarkable 10-fold increase in measurement sensitivity. This enhancement was quantitatively analyzed, providing clear evidence of the effectiveness of MM-ABS integration. The validity of the increased sensitivity was further affirmed through the designed test samples, illustrating that measurements conducted with MM-ABS integration exhibited higher detection capabilities compared to that without MM-ABS.

5.6 Reference

[1] Y. Duan, “Microwave Absorbing Materials.”

[2] M. F. Elmahaishi, R. S. Azis, I. Ismail, and F. D. Muhammad, “A review on electromagnetic microwave absorption properties: their materials and performance,” *Journal of Materials Research and Technology*, vol. 20. Elsevier Editora Ltda, pp. 2188–2220, Sep. 01, 2022. doi: 10.1016/j.jmrt.2022.07.140.

[3] P. Sahoo, L. Saini, and A. Dixit, “Microwave-absorbing materials for stealth application: a holistic overview,” *Oxford Open Materials Science*, vol. 3, no. 1. Oxford University Press, 2023. doi: 10.1093/oxfmat/itac012.

[4] R. Peymanfar *et al.*, “Recent advances in microwave-absorbing materials fabricated using organic conductive polymers,” *Frontiers in Materials*, vol. 10. Frontiers Media S.A., 2023. doi: 10.3389/fmats.2023.1133287.

[5] M. F. Elmahaishi, R. S. Azis, I. Ismail, and F. D. Muhammad, “A review on electromagnetic microwave absorption properties: their materials and performance,” *Journal of Materials Research and Technology*, vol. 20. Elsevier Editora Ltda, pp. 2188–2220, Sep. 01, 2022. doi: 10.1016/j.jmrt.2022.07.140.

[6] N. N. Ghosh, “Editorial: Dielectric microwave absorbing structures,” *Frontiers in Materials*, vol. 10. Frontiers Media S.A., 2023. doi: 10.3389/fmats.2023.1181978.

[7] D. S. Aherrao, C. Singh, and A. K. Srivastava, “Review of ferrite-based microwave-absorbing materials: Origin, synthesis, morphological effects, dielectric/magnetic properties, composites, absorption mechanisms, and optimization,” *Journal of Applied Physics*, vol. 132, no. 24. American Institute of Physics Inc., Dec. 28, 2022. doi: 10.1063/5.0123263.

[8] G. V. Ramesh, S. Porel, and T. P. Radhakrishnan, “Polymer thin films embedded with in situ grown metal nanoparticles,” *Chemical Society Reviews*, vol. 38, no. 9. pp. 2646–2656, 2009. doi: 10.1039/b815242j.

[9] M. Haddadi. M, B. Das, J. Jeong, S. Kim, and D. S. Kim, “Near-maximum microwave absorption in a thin metal film at the pseudo-free-standing limit,” *Sci Rep*, vol. 12, no. 1, Dec. 2022, doi: 10.1038/s41598-022-23119-7.

[10] S. Li *et al.*, “Microwave absorptions of ultrathin conductive films and designs of frequency-independent ultrathin absorbers,” *AIP Adv*, vol. 4, no. 1, Jan. 2014, doi: 10.1063/1.4863921.

[11] N. Janem, Z. S. Azizi, and M. M. Tehranchi, “Microwave absorption and magnetic properties of thin-film Fe3O4 @polypyrrole nanocomposites: The synthesis method effect,” *Synth Met*, vol. 282, Dec. 2021, doi: 10.1016/j.synthmet.2021.116948.

[12] H. Bosman, Y. Y. Lau, and R. M. Gilgenbach, “Microwave absorption on a thin film,” *Appl Phys Lett*, vol. 82, no. 9, pp. 1353–1355, Mar. 2003, doi: 10.1063/1.1556969.

[13] H. Lee, S. Arakelyan, B. Friedman, and K. Lee, “Temperature and microwave near field imaging by thermo-elastic optical indicator microscopy.”

[14] Z. Baghdasaryan *et al.*, “3D visualization of microwave electric and magnetic fields by using a metasurface-based indicator,” *Sci Rep*, vol. 12, no. 1, Dec. 2022, doi: 10.1038/s41598-022-10073-7.

[15] G. V. Ramesh, S. Porel, and T. P. Radhakrishnan, “Polymer thin films embedded with in situ grown metal nanoparticles,” *Chemical Society Reviews*, vol. 38, no. 9. pp. 2646–2656, 2009. doi: 10.1039/b815242j.

[16] H. Bosman, Y. Y. Lau, and R. M. Gilgenbach, “Microwave absorption on a thin film,” *Appl Phys Lett*, vol. 82, no. 9, pp. 1353–1355, Mar. 2003, doi: 10.1063/1.1556969.

[17] H. Lee, S. Arakelyan, B. Friedman, and K. Lee, “Temperature and microwave near field imaging by thermo-elastic optical indicator microscopy,” *Sci Rep*, vol. 6, Dec. 2016, doi: 10.1038/srep39696.

[18] S. Hamelo, J. Yang, and H. Lee, “Detection of Defects in a Dielectric Material by Thermo-Elastic Optical Indicator Microscopy,” *IEEE Access*, vol. 11, pp. 45961–45971, 2023, doi: 10.1109/ACCESS.2023.3274534.

[19] H. Lee, “Detection of Air Bubbles and Liquid Droplet in a Dielectric Tube by Thermo-Elastic Optical Indicator Microscopy,” *IEEE Access*, vol. 10, pp. 33537–33546, 2022, doi: 10.1109/ACCESS.2022.3162247.

[20] Z. Baghdasaryan, A. Babajanyan, L. Odabashyan, H. Lee, B. Friedman, and K. Lee, “Visualization of Microwave Heatingformesh-Patterned Indium-tin-Oxide by a Thermo-Elastic Optical Indicator Microscope,” 2018.

[21] S. Hamelo and H. Lee, “Thickness Dependent Microwave Magnetic Field Heating on Aluminum thin Films by Using Thermo-elastic Optical Indicator Microscopy Method,” *New Physics: Sae Mulli*, vol. 72, no. 1, pp. 19–24, Jan. 2022, doi: 10.3938/NPSM.72.19.

[22] Y. Qi *et al.*, “A tunable terahertz metamaterial absorber composed of elliptical ring graphene arrays with refractive index sensing application,” *Results Phys*, vol. 16, Mar. 2020, doi: 10.1016/j.rinp.2020.103012.

[23] J. Gou, Q. Niu, K. Liang, J. Wang, and Y. Jiang, “Frequency Modulation and Absorption Improvement of THz Micro-bolometer with Micro-bridge Structure by Spiral-Type Antennas,” *Nanoscale Res Lett*, vol. 13, 2018, doi: 10.1186/s11671-018-2484-7.

[24] S. Lai *et al.*, “A High-Performance Ultra-Broadband Transparent Absorber With a Patterned ITO Metasurface,” *IEEE Photonics J*, vol. 14, no. 3, Jun. 2022, doi: 10.1109/JPHOT.2022.3171864.

[25] L. Pometcu, A. Sharaiha, R. Benzerga, P. Pouliguen, and G. Dun, “Improved Microwave Absorption of Pyramidal Absorber Using Metamaterial.”

[26] C. M. Watts, X. L. Liu, and W. J. Padilla, “Metamaterial Electromagnetic Wave Absorbers,” 2002.

[27] *2008 International Workshop on Metamaterials.* I E E E, 2008.

[28] H.-M. Lee and H.-S. Lee, “A METAMATERIAL BASED MICROWAVE ABSORBER COMPOSED OF COPLANAR ELECTRIC-FIELD-COUP-LED RESONATOR AND WIRE ARRAY,” 2013.

[29] M. Amiri, F. Tofigh, N. Shariati, J. Lipman, and M. Abolhasan, “Review on Metamaterial Perfect Absorbers and Their Applications to IoT,” *IEEE Internet of Things Journal*, vol. 8, no. 6. Institute of Electrical and Electronics Engineers Inc., pp. 4105–4131, Mar. 15, 2021. doi: 10.1109/JIOT.2020.3025585.

[30] W. Li, M. Xu, H. X. Xu, X. Wang, and W. Huang, “Metamaterial Absorbers: From Tunable Surface to Structural Transformation,” *Advanced Materials*, vol. 34, no. 38. John Wiley and Sons Inc, Sep. 01, 2022. doi: 10.1002/adma.202202509.

[31] Y. I. Abdulkarim *et al.*, “A Review on Metamaterial Absorbers: Microwave to Optical,” *Frontiers in Physics*, vol. 10. Frontiers Media SA, Apr. 29, 2022. doi: 10.3389/fphy.2022.893791.

[32] P. Yu *et al.*, “Broadband Metamaterial Absorbers,” *Advanced Optical Materials*, vol. 7, no. 3. Wiley-VCH Verlag, Feb. 05, 2019. doi: 10.1002/adom.201800995.

[33] S. Qu, Y. Hou, and P. Sheng, “Conceptual-based design of an ultrabroadband microwave metamaterial absorber,” vol. 118, 2021, doi: 10.1073/pnas.2110490118/-/DCSupplemental.

[34] C. Cen *et al.*, “High quality factor, high sensitivity metamaterial graphene—perfect absorber based on critical coupling theory and impedance matching,” *Nanomaterials*, vol. 10, no. 1, Jan. 2020, doi: 10.3390/nano10010095.

[35] K. Fan and W. J. Padilla, “Dynamic electromagnetic metamaterials,” in *Materials Today*, Elsevier B.V., Jan. 2015, pp. 39–50. doi: 10.1016/j.mattod.2014.07.010.

Chapter highlights

This chapter presents an innovative approach for mapping the permittivity of dielectric materials. This method works by incorporating metamaterial absorbers into thermoelastic optical indicator microscopy measurement system. The experimental setup, working principle of the metamaterial integrated approach, and underlying measurement techniques are discussed in detail in this chapter. Practical demonstrations are used to show the potential of this approach for the characterization of various dielectric materials.

CHAPTER 6

Non-destructive dielectric measurement and mapping using metamaterial integrated TEOIM.

6.1 Introduction

The ability to map the dielectric constant of materials provides a significant advantage to understand their electrical properties and performance. This advantage is the foundation for a variety of applications, including characterization of materials [1]– [3], quality control in manufacturing [4]– [6], studying the dielectric properties of biological tissue in biomedical research [7]– [9], evaluating electronic device performance [2], [3], [10], [11], and identifying material defects [12]–[19]. In these applications, techniques operating in the microwave frequency range are particularly useful because they can penetrate with low loss and provide valuable information about their internal structure and composition. Additionally, microwave techniques offer the advantage of being non-destructive, allowing for repeated measurements without damaging the sample. This makes them ideal for continuous monitoring and real-time analysis. [13], [16], [18], [20], [21].

Recently, these techniques have been combined with metamaterials to improve the testing and characterization of dielectric materials [22]– [29]. Among these, an array of metamaterial structures has shown promise for mapping the spatial permittivity of dielectric materials [30]– [38]. For example, an array of metamaterial structures exited by the transmission line operating at different resonant frequencies have been reported [7], [33], [39]. In this method, the desired dielectric material is positioned near the structures. The interaction between the resonators and the dielectric material leads to changes in the transmission properties, thus facilitating the mapping of the permittivity distribution within the sample. However, the resolution is non-uniform due to restrictions imposed by the size of

the resonant frequency of the metamaterial structure on the transmission line. In addition, microwave near-field microscopy and microwave holography have also been reported [35], [40], but they involve time-consuming aspects related to scanning.

In this work, a new approach to measure the permittivity of the dielectric material is presented. The proposed method is based on the integration of a metamaterial absorber (MM-ABS) with thermoelastic optical indicator microscopy (TEOIM). TEOIM is a high-resolution microwave near-field measurement technique that does not require scanning [41]–[47]. By using the resonant properties of the metamaterial absorbers, the permittivity distribution of dielectric materials can be determined. Metamaterial absorbers are two-dimensional arrays of resonator structures fabricated on a dielectric substrate [48]. These absorbers are characterized by strong resonant properties. Due to these resonant properties, they produce strong, measurable signals characterized by an absorption peak. This absorption peak is significant enough to accurately monitor shifts in frequency when metamaterials are exposed to external influences that change the dielectric environment. This dielectric environment changes the electromagnetic properties accordingly and leads to changes in the resonant frequency [49]– [51]. Therefore, by integrating the metamaterial with the optical indicator (OI), the peaks of resonance intensity at the resonance frequency can be measured using the existing TEOIM measurement principle. OI is a component of TEOIM, it is a glass substrate coated with a thin film that provides an optical signal in response to the absorption of the microwave signal.

To achieve this, MM-ABS consists of 36 x 36 array of resonators distributed on a 100 x 100 alumina substrate were fabricated. All resonating at 11.5 GHz and each resonator is decoupled from their neighbor resonator by an optimized pacing. The distributed resonators are sensing units whose resonant frequency shift is a function of the permittivity change in

their specific locations. To evaluate this, test samples with different dielectric constants were fabricated. Their microwave near-field distribution was measured by placing the test samples on the metamaterial. Based on their resonant frequency, a characteristic equation that relates the dielectric constant to the resonant frequency was formulated. The obtained result was then used to map the dielectric constant using the LabVIEW program.

6.2 Experiment.

6.2.1 Design, simulation, and fabrication of metamaterial absorber.

The simulation experiments were conducted using the CST Microwave Studio Suite, 2019. Figure 6.1(a) shows the simulation setup in the software. The unit cell is simulated in an infinite periodic structure with unit cell boundary conditions along the x and y directions, an open space, and a PEC at the front of the metamaterial. Figure 6.1(b) illustrates the structure of the unit cell, which is a modification of the complementary rectangular split ring resonator. This modification involves connecting the outer and inner rectangular rings and symmetrically inserting a strip into the inner ring to achieve the small dimensions of the unit cell for the required frequency range.

In the simulation environment, an alumina substrate (εr = 9.8) and silver were used for the metal pattern, with a conductivity of 6.3× 107 S/m. Systematically varying the dimensions of the resonator allowed the observation of resonance characteristics. The dimensions were successfully determined through optimization, resulting in a resonance frequency of 11.56 GHz. The main parameters of the structure, including gap width (g), substrate length (h), line width (w), length of structure (l), and thickness of substrate (t), are presented in the following figure: g = 0.1mm, h = 2mm, w = 0.1mm, l = 1.2mm, and t = 1mm.

Upon completion of the unit cell structure design, the metamaterial was printed on a 100 mm x 100 mm alumina substrate. The printing process was carried out using a laser machine (JTY Fiber 20) after applying silver paste in the first step. Then, the printed structure went through a 3-hour drying process in the furnace (SH-FU-5MG) at a temperature of 800 degrees Celsius to ensure strong adhesion between the metal structure and the substrate. The fabricated metamaterial plate is presented in Figure 6.1 (c).

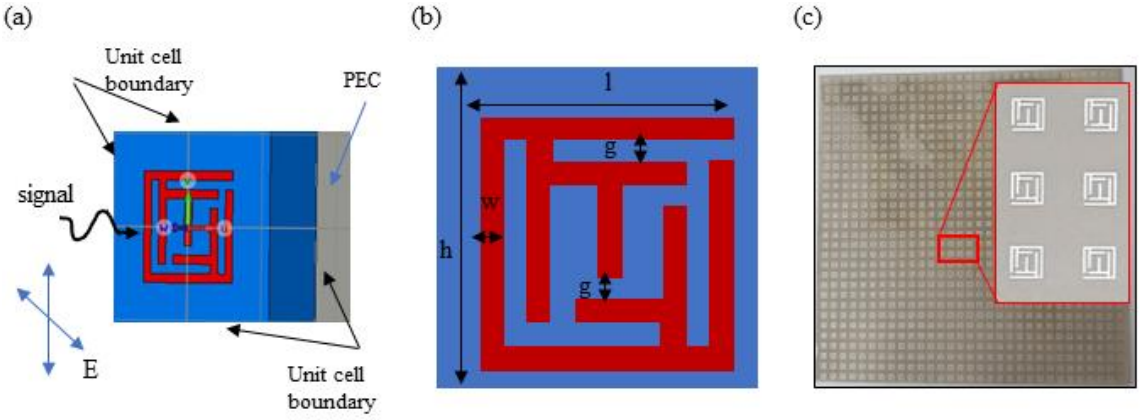

Figure 6.1. (a) Simulation setup (b) Illustration of the unit cell (c) The metamaterial plate and its magnified view.

6.2.2 Validation of decoupled resonators of MM-ABS through CST simulation.

After designing the unit cell of the MM-ABS, the optimal separation where the coupling of the resonators is minimized was determined by simulating various distances between the resonators. Figure 6.2 (a) displays the results of the reflection coefficient for a single unit cell and an array of unit cells at a separation of 1.6 between the resonators. In the simulation setup, the boundary condition for a single unit cell was the perfect electric boundary (PEC) in the x-direction, and the perfect magnetic boundary (PMC) was introduced in the y-direction. An open space (with added space) was utilized, along with a PEC (Perfect Electric Conductor) at the front of the metamaterial. For the array of unit cells within the periodic structure, the unit cell was considered infinite along the x and y directions, with open space

(with added space) and a PEC at the front of the metamaterial. The resonant frequency of both single and arrayed unit cells remained unchanged. This observation indicates that the coupling between the resonators is negligible. Therefore, the resonator can respond independently at this optimized separation. Besides the optimized distance between the resonators, the design of the unit cell contributed to the resonator's negligible coupling.

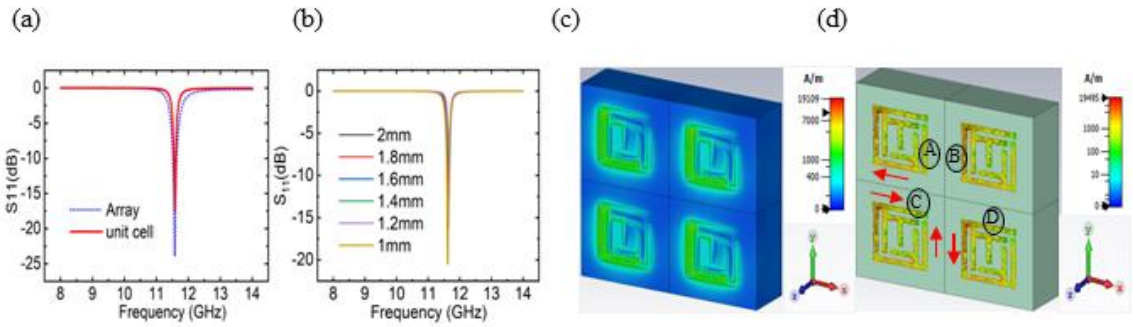

Figure 6.2 (a) The results of the reflection coefficient of single and array resonators. (b) Reflection coefficient for different distances between the resonators. (c) The magnetic field distribution of the array structure (d) the surface current distribution of the array structure.

This is because the current flows in opposite directions on the neighboring resonator sides, as illustrated in Figure 6.2 (d) A, B, C, and D, thereby eliminating coupling effects. Furthermore, Figure 6.2 (c) demonstrates that the field distributions are confined to the unit cell, providing another indication that the unit cells have no interference with the surrounding structures.

6.2.3 Experimental setup and working principle.

Figure 6.3 (a) shows the experimental setup of TEOIM to measure the microwave near-field distribution with metamaterial absorber (MM-ABS). The magnified view in Figure 6.3 (a) shows the sample on the array of resonators. Figure 6.3 (b) shows the configuration of the MM-ABS with OI. The OI is a glass substrate coated with the ITO thin film.

For dielectric mapping, the principle of operation of the MM-ABS is that each resonator represents one pixel of the dielectric image of the MUT to obtain a one-cell resolution. For this purpose, all pixels resonate at the same frequency but are not coupled with their neighbors. Therefore, the measured near-field distribution gives independent absorption peaks at specific locations. When the DUT is placed on the MM-ABS, the field on the resonator is influenced by the dielectric properties of the DUT. This results in a shift in the resonance frequency of the resonator. By analyzing these frequency shifts, the dielectric permittivity can be determined.

The OI used in the measurement is a glass substrate coated by ITO coated thin films. Since the ITO is conductive material the visualized field distribution and intensity picks refer to the microwave magnetic fields (H-MWMNF).

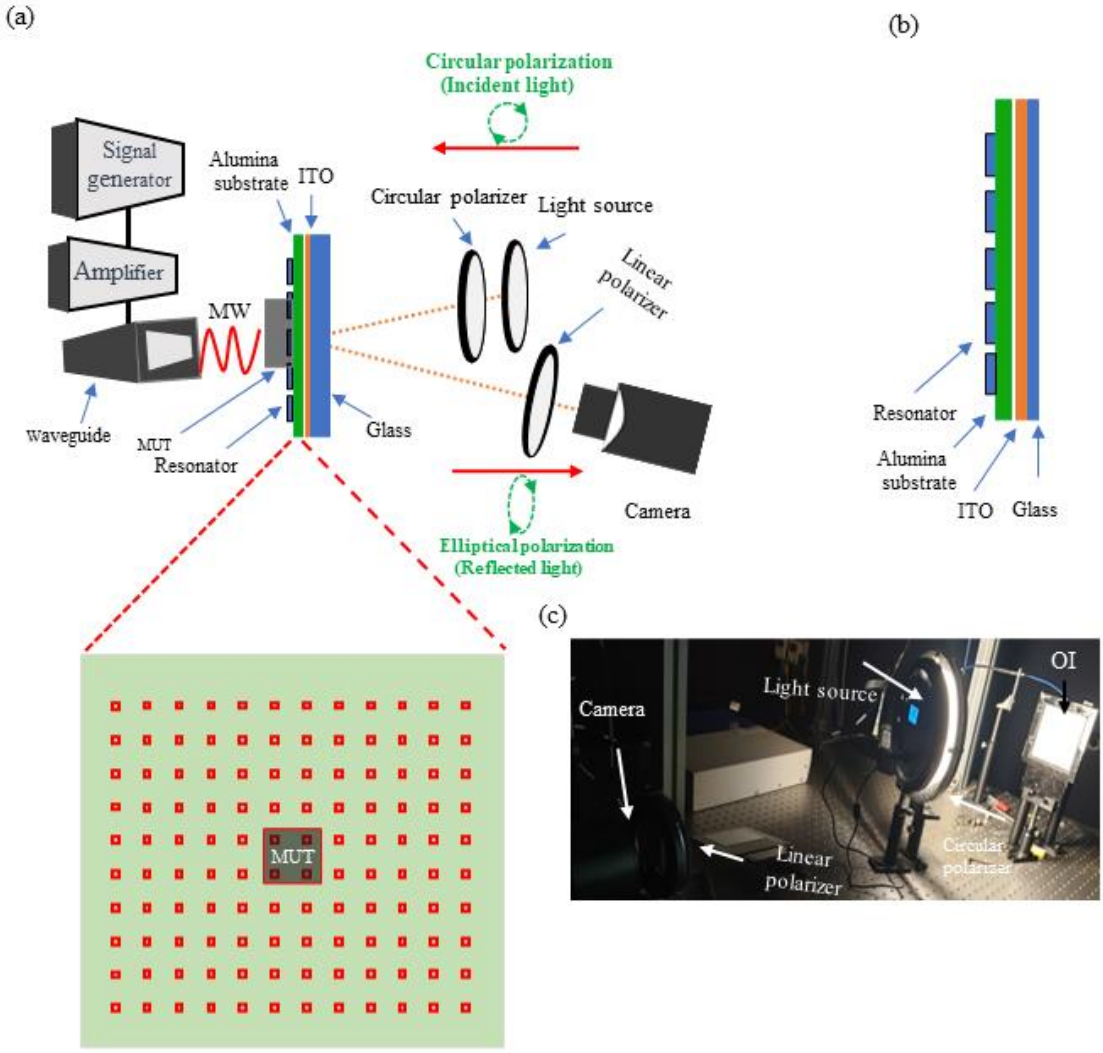

Figure 6.3. (a) Illustration of the measurement setup of MM-ABS integrated with TEOIM for H-MWMNF distribution measurement, the enlarged portion shows the MUT placed on the resonators. (b) shows the configuration of MM-ABS with the OI. (c) shows photos of the measurement setup.

6.3 Result and discussion

6.3.1 Microwave near-field measurement.

For spatial dielectric mapping using the MM-ABS integrated TEOIM technique, the metamaterial resonators respond independently at their respective locations. To evaluate this,

the H-MWNF distribution measurements were performed using the measurement setup 6.3 (a) in a frequency range from 8 GHz to 14 GHz and the OI and MM-ABS configuration shown in Figure 6.3 (b).

Figure 6.4 (a) shows the result of the intensity line profile across the MM-ABS at 11.5 GHz. Figure 6.4 (b) shows the result of the intensity as a function of frequency. Figure 6.4 (c) shows the simulated reflection coefficient. Figure 6.4 (d) shows the microwave near-field distribution measured with the MM-ABS, while (e) shows the H-MWNF measured without the MM-ABS.

The field distribution result in Figure 6.4 (d) shows distributed spots in all the measured frequencies with MM-ABS compared to the field distribution measurement without MM-ABS Figure 6.4 (e). However, in Figure 6.4 (d) at 11.5 GHz strong field spots are observed compared to other frequencies. These spots indicate the independent absorption peaks of each resonator at the resonant frequency, which is indicative of the resonant frequency of the MM-ABS at 11.5 GHz and highlights the resonant properties of the MM-ABS.

The measured result of intensity as a function of frequency change in Figure 6.4 (b) and the simulated results of the reflection coefficient in Figure 6.4 (c) confirmed that the designed MM-ABS resonates around 11.5 GHz.

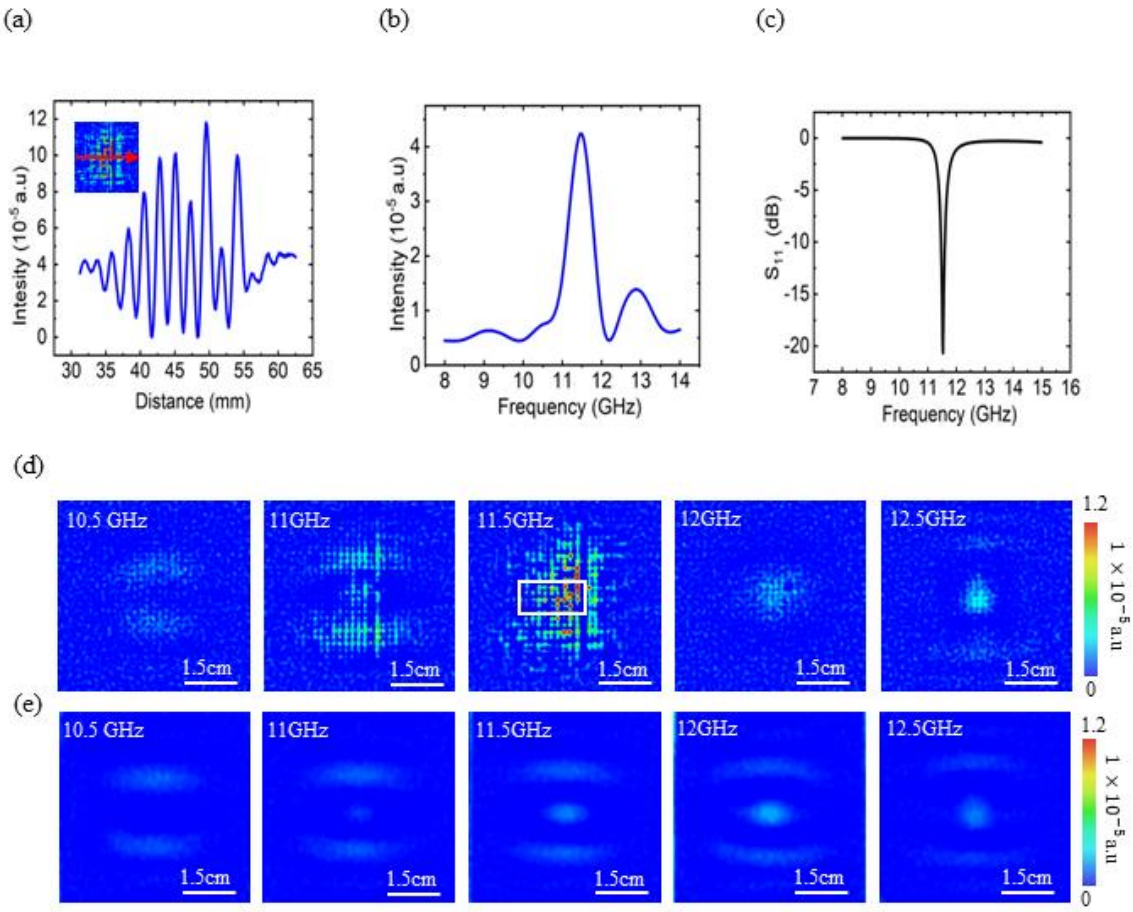

Figure 6.4 The experiment to determine the resonance properties of MM-ABS (a) the intensity line profile measured via MM-ABS at the resonance frequency.(b) the intensity as a function of frequency (c) the result of the simulated reflection coefficient (d) the H-MWNF distribution measured with MM-ABS (e) the H-MWNF distribution measured without MM -ABS.

The intensity line profile calculated across the resonator at the resonance frequency showed the resonators have maximum picks at the resonator location and minimum picks between the resonators, as shown in Figure 6.4 (a). This behavior is compelling evidence of the non-coupling nature of the resonators at the resonance frequency. Here, the intensities are stronger in the center of the MM-ABS. This is because the waveguide is located in the center of MM-ABS therefore H-MWNF distribution is strongest in the center compared to outside the center of the MM-ABS. The non-coupling property of MM-ABS in Figure 6.4 (a) is of

paramount importance for spatial dielectric mapping. As each resonator operates autonomously, it serves as a unique pixel for dielectric mapping, ensuring precise detection of electromagnetic properties at specific locations.

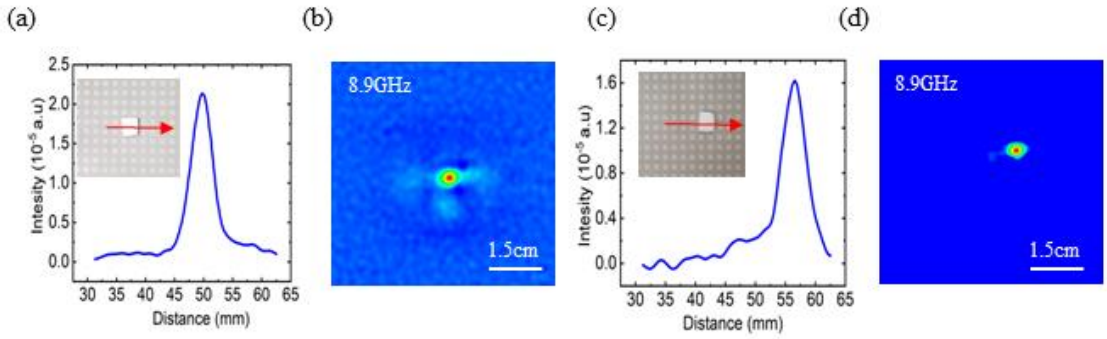

Figure 6.5 An experiment was performed to evaluate the MM-ABS when the test sample placed at different positions. (a) and (c) the intensity line profile when the test sample is at the center of MM-ABS and shifted from the center (b) and (d) the H-MWNF distribution when the test sample is at the center and moved to the right

To evaluate the consistency of the response of the resonators at different positions of MM-ABS, a test sample of alumina, measuring 4mm x 3mm, was introduced at two distinct locations. The first measurement involved placing the sample in the center of MM-ABS, and the second measurement involved shifting the position to the right. In both scenarios, the H-MWNF distribution was measured. Figures 6.5 (a) and (c) display the results of the intensity line profile when the test sample is introduced at the center of the MM-ABS and shifted to the right from the center. Figure 6.5 (b) and (d) present the results of the microwave near-field distribution when the sample is placed at the center and shifted from the center. The results from the intensity line profile and the microwave field distribution reveal a strong field distribution at the resonators located where the test sample was placed. In contrast, the remaining resonators exhibit a uniformly weak field distribution. Importantly, this strong

field distribution was consistently observed at 8.9 GHz in both positions. The results indicate that the MM-ABS demonstrates remarkable stability in response across varied positions.

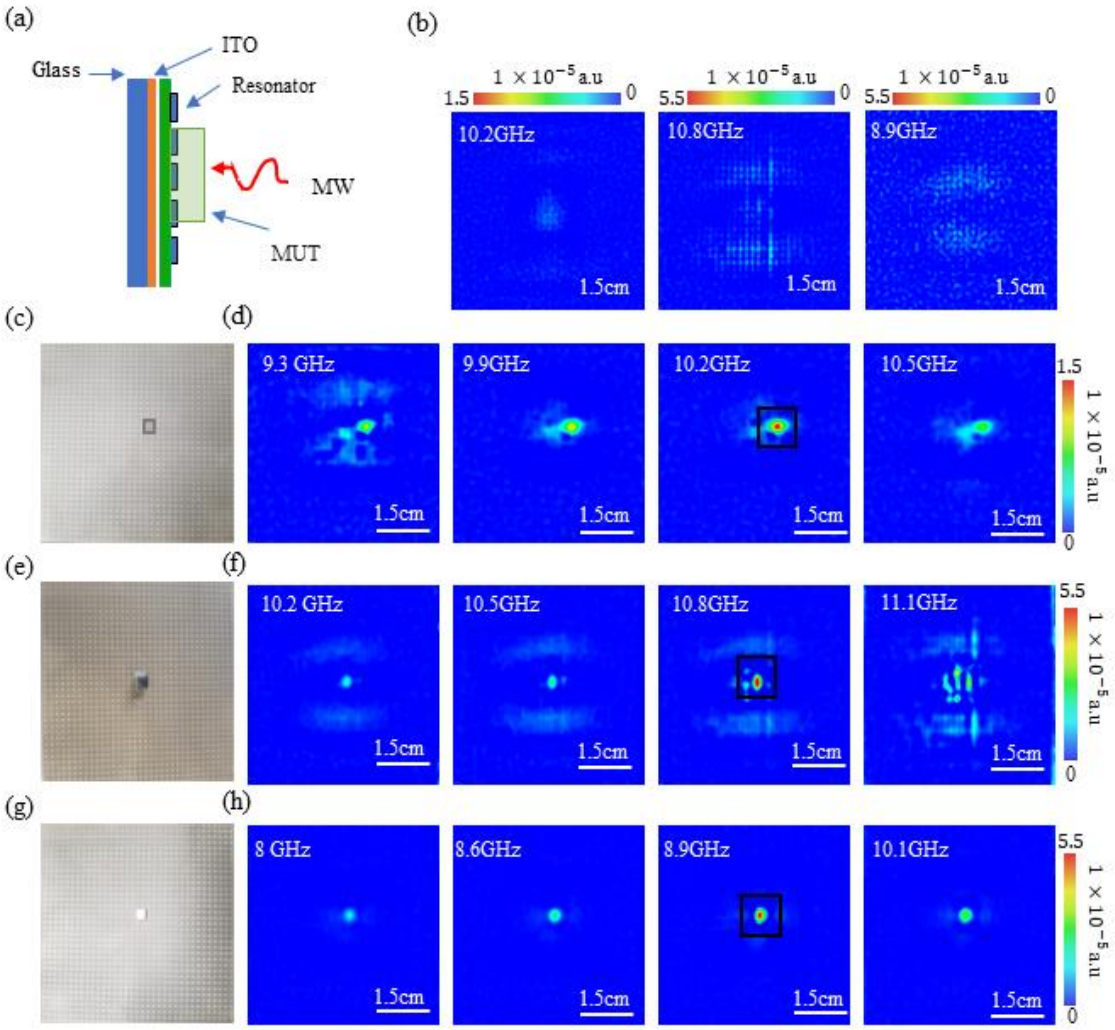

Figure 6.6 The experimental result of microwave H-MWNF to evaluate the performance of the MM-ABS when different dielectric materials were placed. (c), (e) and (g) show the test samples on the MM-ABS during the measurement. (b) The results of H-MWNF distribution without introducing the test sample on the metamaterial. (d), (f) and (h) is results of H-MWNF by introducing the glass, acrylic and alumina a test sample respectively on the MM-ABS

To investigate the response of MM-ABS to materials with different dielectric constants, a series of experiments were conducted based on the configuration in Figure 6.6 (a). In each experiment, various dielectric materials, each with its own specific dielectric constant, were placed on the MM-ABS. The test sample included alumina (ε_r=9.8) as shown in Figure 6.6 (g), acrylic (ε_r=3) as shown in Figure 6.6 (e), and glass (ε_r=5) as shown in Figure 6.6 (c). For reference, measurements were also performed without test samples (ε_r =1).The microwave near-field distribution was measured for each material in a frequency range from 8 GHz to 14 GHz, and the dimensions of the test sample were 3mm by 4mm.

Based on these experiments, Figure 6.6 (b) shows the results of the measured H-MWNF distribution without the test sample; Figure 6.6 (d) shows the results of the measured H-MWNF distribution of the glass sample; Figure 6.6 (f) shows the results of the measured H-MWNF distribution of the acrylic sample; and Figure 6.6 (h) exhibits the results of the measured H-MWNF distribution of the alumina sample.

The experiments revealed the resonant frequency characteristics of the MM-ABS when different dielectric materials were placed on it. Specifically, the resonant frequency for air (without test sample) was measured at 11.5 GHz, aligning with the intended resonant frequency of the MM-ABS. A frequency shift from 11.5 GHz to 8.9 GHz was detected for the alumina sample. The acrylic test sample exhibited a shift in resonant frequency to 10.8 GHz, while the glass showed a frequency shift of 10.2 GHz. These resonance frequency shifts demonstrate that the resonant response of MM-ABS is influenced by the dielectric properties of the test sample, showing MM-ABS capacity to detect variations in dielectric constants. These results emphasize the sensitivity of MM-ABS in identifying and responding to materials with varying dielectric constants. Moreover, it was observed that dielectric materials with higher dielectric constants induced more substantial frequency shifts. The

above result is confirmed by the calculated intensity as the function of frequency shown in Figure 6.7 (a) and the simulated reflection coefficient result in Figure 6.7 (b).

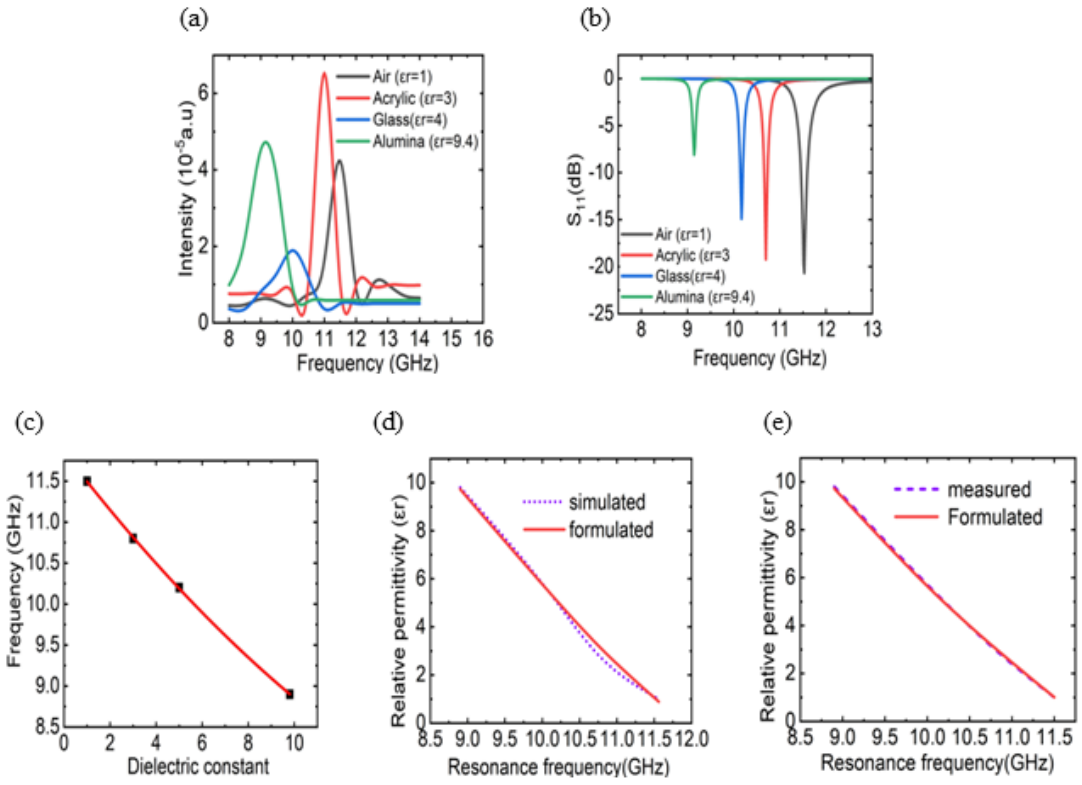

Figure 6.7 (a) the H-MWNF of the samples (b) the simulated reflection coefficient for the samples (c) the fitting curve with the measured result. (d) and (e) a comparison of the measured and simulated dielectric constant with the formulated fitting equations.

To evaluate the ability of MM-ABS to discriminate between different dielectric materials when placed simultaneously in different locations, an experiment was conducted. In this experiment, three different dielectric samples such as alumina, acrylic, and glass were positioned at different locations on the MM-ABS, as shown in Figure 6.8 (a). The H-MWNF was measured over a frequency range from 8 GHz to 14 GHz.

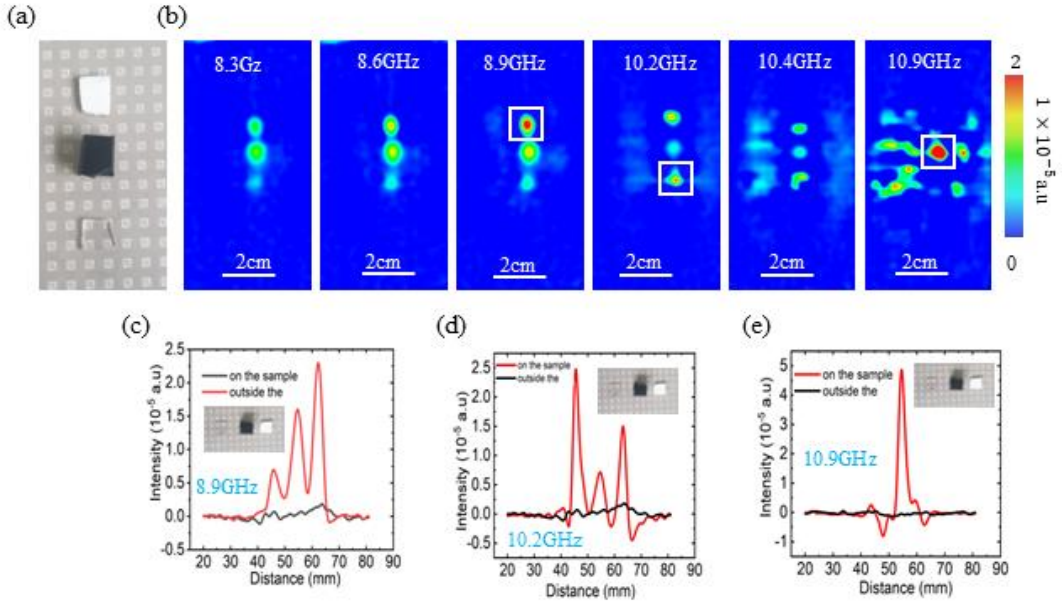

Figure 6.8 simultaneously measured H-MWNF distribution of the three samples (a) images of the three samples on the MM-ABS (b) The H-MWNF of the three samples. (b) The intensity line profile of the three samples at the frequency of 8.9 GHz, 10.2 GHz, and 10.9 GHz.

The results of the experiment show a clear pattern. Each sample shows a strong microwave near-field distribution response at different frequencies. In particular, the alumina sample showed a strong field distribution at 8.9 GHz, the acrylic plate at 10.9 GHz, and the glass sample at 10.2 GHz. This result emphasizes the ability of MM-ABS to distinguish between dielectric variations in a single measurement. These results are consistent with previously independently measured results, further validating the methodology and increasing its reliability. The intensity line profile confirms the measured near-field distribution and shows that each test sample has distinct peaks at the corresponding resonant frequencies. These results are of great importance for the application of spatial permittivity mapping as they effectively reveal the dielectric variations within different positions of a sample through a single measurement.

6.3.2 Equation Formulation

To establish a quantitative relationship between the dielectric constant (ε_r) of the materials and the corresponding resonant frequency ($f_{r,\,MUT}$) of the resonator, a numerical analysis was performed using the measured data to derive an equation that shows this correlation. To achieve this, a polynomial function was used with fitting parameters expressed by the equation.

$$f_{r,MUT} = A_1 + A_2\varepsilon_r + A_3{\varepsilon_r}^2 \qquad 6.1$$

Where $f_{r,\,MUT}$ represents the resonant frequency of each resonator on the MM-ABS, while ε_r is the dielectric constant of the material under study. Three fitting parameters enter the equation. A_1, A_2, and A_3, which are used to approximate the relationship between dielectric constant and resonant frequency.

The equation for calculating the dielectric constant (ε_r) based on the resonance frequency ($f_{r,\,MUT}$) is presented as follows.

$$\varepsilon_r = 0.3657 + \frac{\sqrt{0.1337 - 0.252(11.86 - f_{r,MUT})}}{0.0126} \qquad 6.2$$

This equation allows for the estimation of the dielectric constant of a material by inputting its resonance frequency. In Figure 6.7 (c), the corresponding fitting curve is displayed, offering a visual representation of how the equation fits the experimental and simulated data points. The close agreement between the calculated values and the simulated values is shown in Figure 6.7 (d), and the measured values and calculated values are shown in Figure 6.7 (c).

6.3.3 **Dielectric mapping**

A customized LabVIEW program was used to create comprehensive dielectric maps of the samples using the formulated equation that links the dielectric constants to the resonant frequencies of each resonator on MM-ABS. Steps for the LabVIEW program is illustrated in Figure 6.13 (a).

Figure 6.9 illustrates the measuring procedure of the dielectric permittivity of the sample placed on the MM-ABS. Assuming three test samples placed on the MM-ABS, their H-MWNF distribution was measured. The resonance frequency was determined from the H-MWNF measurement and finally, the permittivity of the test sample was measured based on the formulated equation.

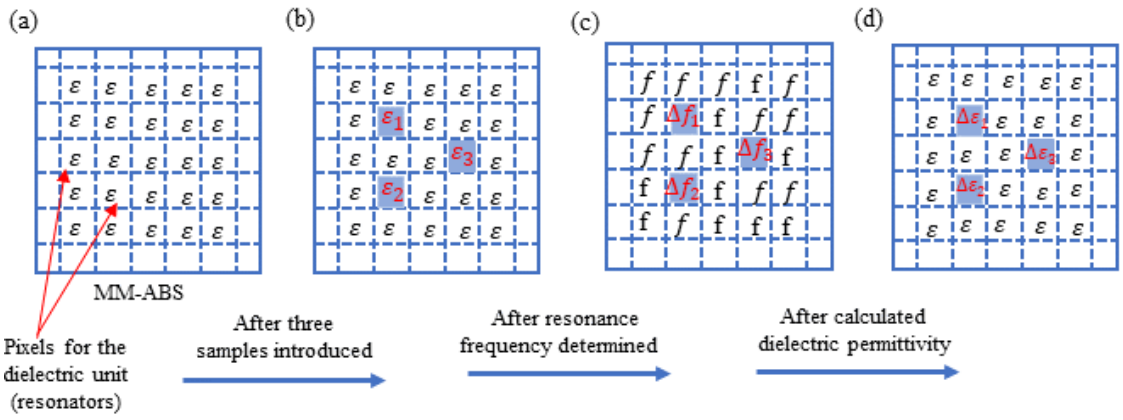

Figure 6.9. An illustration for the process of dielectric mapping using MM-ABS (a) each resonator representing pixels of the dielectric unit (b) a test sample placed on the resonators (c) measured frequency shift for each resonator. (d) the imaged permittivity of each dielectric resonators based on their resonant frequency

To image the dielectric permittivity of the test samples based on the above procedure, the microwave near-field image results of the three samples, namely alumina, acrylic, and glass, were separately fed to the custom-designed LabVIEW program. Figures 6.6 (c), (e), and (g)

are the spatial locations where the test samples were placed on the MM-ABS, and the field distribution images at the resonant frequencies were used to calculate the dielectric permittivity of each sample. Based on this, Figure 6.10 (a), (b), and (c) are the calculated images of the dielectric permittivity of glass, acrylic, and alumina test samples respectively.

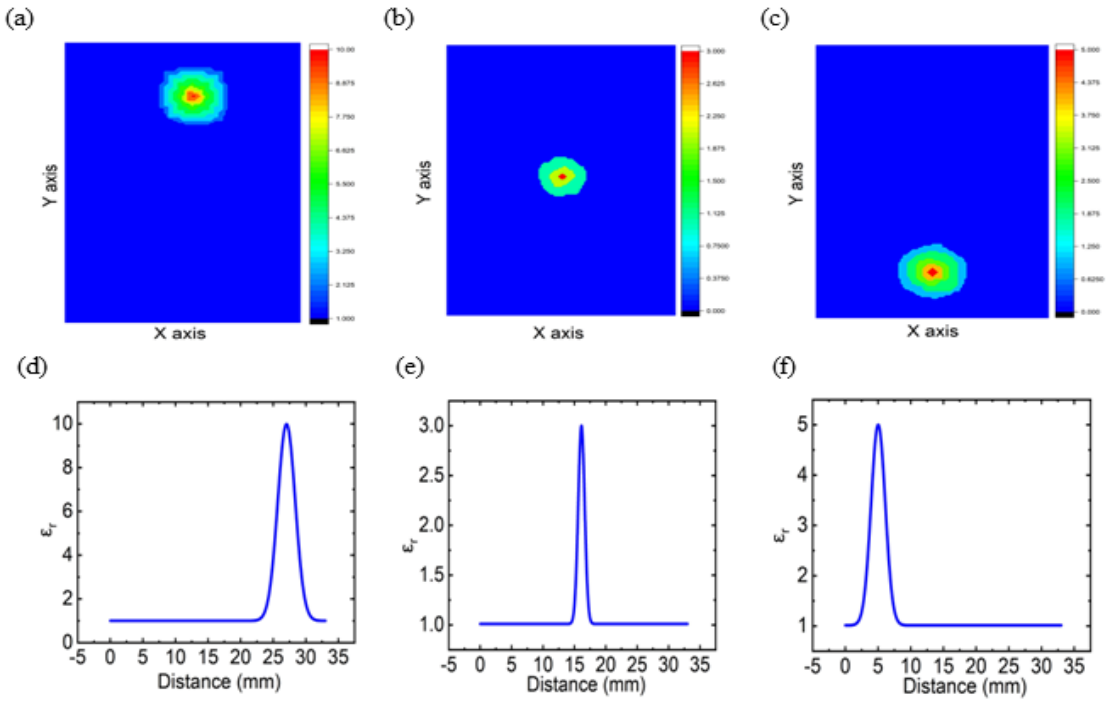

Figure 6.10. the imaged permittivity of individual sample and their line profile (a) Alumina sample. (b) Acrylic sample (c) Glass sample. (d-f) permittivity line profile of alumina, acrylic, and glass samples.

Figures 6.10 (d), (e), and (f) show permittivity line profiles that provide insight into the variations of dielectric constants along specific paths within the samples.

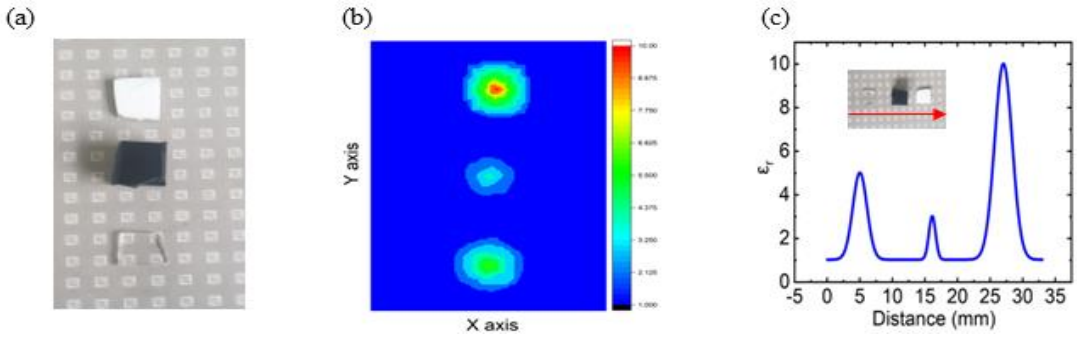

Figure 6.11. simultaneously imaged permittivity of different dielectric constant and their line profile. (a) Photographs of the three samples (b) Simultaneously measured dielectric values of the samples shown. (c) Dielectric line profile across the three samples

To further demonstrate the applicability of the methodology for simultaneously imaging dielectric samples with distinct permittivity values, measurements were conducted on samples with different dielectric constants placed on the MM-ABS. Figure 6.10(a) provides an image of the three samples positioned on the MM-ABS, while Figure 6.10(b) displays the mapped permittivity of these samples. Additionally, Figure 6.10 (c) presents the permittivity line profile. The results of these permittivity measurements for diverse dielectric samples show the effectiveness of the methodology. This capability holds significant implications, particularly in scenarios involving materials with spatial variations in dielectric properties. The successful mapping of different dielectric samples simultaneously suggests practical utility in a non-destructive way across various applications, ranging from material characterization and quality control to biomedical research and defect identification. Furthermore, the methodology represents an accurate approach to determining the dielectric properties of complex dielectric materials.

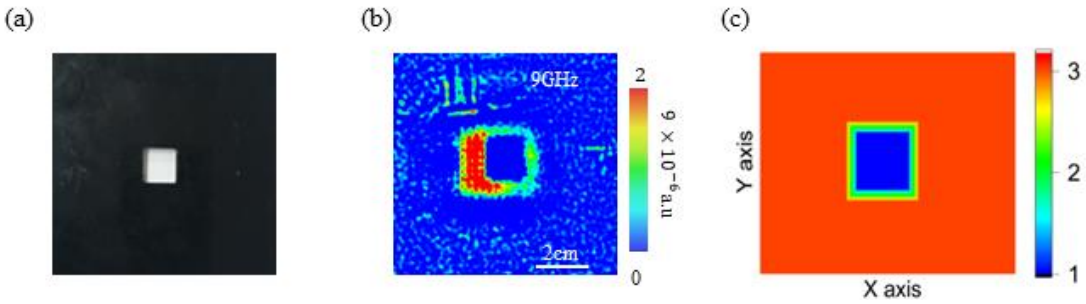

Figure 6.12. permittivity images of rectangular hole (a) Photographs Acrylic plate (b) measured H-MWNF distribution (c) mapped dielectric permittivity.

To further validate the methodology, a test sample with a known shape was employed. This test sample was a 100 mm x 100 mm square acrylic plate featuring a 1.5 mm x 1.5 mm rectangular hole. Figure 6.11(a) provides an image of this rectangular acrylic plate. Figure 6.11(b) presents the imaged microwave near-field distribution, while Figure 6.11(c) displays the mapped dielectric distribution of the sample. The successful mapping of the known features within the test sample validates the effectiveness of the proposed methodology.

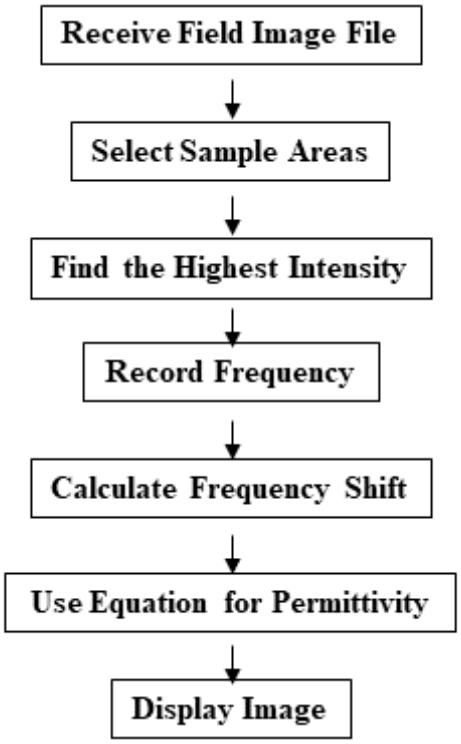

Figure 6.13 Steps in a LabVIEW program for mapping a dielectric object.

6.4 Conclusion.

In conclusion, this chapter introduced a new approach that integrates thermoelastic optical indicator microscopy (TEOIM) with metamaterial absorbers (MM-ABS) for dielectric mapping. That involves fabricating MM-ABS, consisting of a 36 x 36 array of resonators, all operating at a resonant frequency of 11.5 GHz. The H-MWNF measurement showed spatially distributed absorption peaks, indicating that each resonator of the MM-ABS is independently resonating at 11.5 GHz. When the test sample was placed in a different position on the MM-ABS, it exhibited a consistent response and was able to distinguish between different dielectric constant samples through simultaneous measurement via its frequency shift response and H-MWNF distribution measurement. Based on the response of the frequency shift, an equation was formulated that relates the dielectric constant of the material to the resonance frequency. Using the LabVIEW program, the permittivity of the dielectric constant is imaged. This technique holds promise for various applications, providing a non-destructive and efficient means of mapping dielectric properties and eliminating the need for time-consuming scanning.

6.5 Reference

[1] S. Giordano, “Dielectric and elastic characterization of nonlinear: Heterogeneous materials,” *Materials*, vol. 2, no. 4. pp. 1417–1479, 2009. doi: 10.3390/ma2041417.

[2] P. Bøggild *et al.*, “Mapping the electrical properties of large-area graphene,” *2D Materials*, vol. 4, no. 4. IOP Publishing Ltd, Dec. 01, 2017. doi: 10.1088/2053-1583/aa8683.

[3] K. I. Tifkitsis and A. A. Skordos, “A novel dielectric sensor for process monitoring of carbon fibre composites manufacture,” *Compos Part A Appl Sci Manuf*, vol. 123, pp. 180–189, Aug. 2019, doi: 10.1016/j.compositesa.2019.05.014.

[4] D. El Khaled, N. Novas, J. A. Gazquez, R. M. Garcia, and F. Manzano-Agugliaro, “Fruit and vegetable quality assessment via dielectric sensing,” *Sensors (Switzerland)*, vol. 15, no. 7. MDPI AG, pp. 15363–15397, Jun. 29, 2015. doi: 10.3390/s150715363.

[5] S. K. Pankaj *et al.*, “Characterization of polylactic acid films for food packaging as affected by dielectric barrier discharge atmospheric plasma,” *Innovative Food Science and Emerging Technologies*, vol. 21, pp. 107–113, 2014, doi: 10.1016/j.ifset.2013.10.007.

[6] S. N. Jha *et al.*, “Measurement techniques and application of electrical properties for nondestructive quality evaluation of foods-a review,” *Journal of Food Science and Technology*, vol. 48, no. 4. pp. 387–411, Aug. 2011. doi: 10.1007/s13197-011-0263-x.

[7] C. Gabriel, S. Gabriel, and E. Corthout, “The dielectric properties of biological tissues: I. Literature survey,” 1996.

[8] K. Sasaki, E. Porter, E. A. Rashed, L. Farrugia, and G. Schmid, “Measurement and image-based estimation of dielectric properties of biological tissues - Past, present, and future - Past, p,” *Phys Med Biol*, vol. 67, no. 14, Jul. 2022, doi: 10.1088/1361-6560/ac7b64.

[9] G. H. Markx and C. L. Davey, “The dielectric properties of biological cells at radiofrequencies: Applications in biotechnology,” 1999.

[10] F. Palumbo *et al.*, “A Review on Dielectric Breakdown in Thin Dielectrics: Silicon Dioxide, High-k, and Layered Dielectrics,” *Advanced Functional Materials*, vol. 30, no. 18. Wiley-VCH Verlag, May 01, 2020. doi: 10.1002/adfm.201900657.

[11] J. T. Anderson *et al.*, “Solution-processed HafSOx and ZircSOx inorganic thin-film dielectrics and nanolaminates,” *Adv Funct Mater*, vol. 17, no. 13, pp. 2117–2124, Sep. 2007, doi: 10.1002/adfm.200601135.

[12] A. Kumari, S. P. Singh, N. K. Tiwari, and M. J. Akhtar, “Design of a Differential Spoof Surface Plasmon Sensor for Dielectric Sensing and Defect Detection,” *IEEE Sens J*, vol. 22, no. 4, pp. 3188–3195, Feb. 2022, doi: 10.1109/JSEN.2022.3142067.

[13] H. Zhang, R. Yang, Y. He, A. Foudazi, L. Cheng, and G. Tian, “A review of microwave thermography nondestructive testing and evaluation,” *Sensors (Switzerland)*, vol. 17, no. 5. MDPI AG, May 15, 2017. doi: 10.3390/s17051123.

[14] P. Casacuberta, J. Muñoz-Enano, P. Vélez, L. Su, M. Gil, and F. Martín, “Highly sensitive reflective-mode defect detectors and dielectric constant sensors based on open-ended stepped-impedance transmission lines,” *Sensors (Switzerland)*, vol. 20, no. 21. MDPI AG, pp. 1–12, Sep. 01, 2020. doi: 10.3390/s20216236.

[15] M. Gil, P. Velez, F. Aznar-Ballesta, J. Munoz-Enano, and F. Martin, “Differential Sensor Based on Electroinductive Wave Transmission Lines for Dielectric Constant Measurements and Defect Detection,” *IEEE Trans Antennas Propag*, vol. 68, no. 3, pp. 1876–1886, Mar. 2020, doi: 10.1109/TAP.2019.2938609.

[16] N. H. M. M. Shrifan, M. F. Akbar, and N. A. M. Isa, “Prospect of using artificial intelligence for microwave nondestructive testing technique: A review,” *IEEE Access*, vol. 7, pp. 110628–110650, 2019, doi: 10.1109/ACCESS.2019.2934143.

[17] N. H. M. M. Shrifan, G. N. Jawad, N. A. M. Isa, and M. F. Akbar, “Microwave Nondestructive Testing for Defect Detection in Composites Based on K-Means Clustering

Algorithm," *IEEE Access*, vol. 9, pp. 4820–4828, 2021, doi: 10.1109/ACCESS.2020.3048147.

[18] D. A. Tonga *et al.*, "Nondestructive Evaluation of Fiber-Reinforced Polymer Using Microwave Techniques: A Review," *Coatings*, vol. 13, no. 3. MDPI, Mar. 01, 2023. doi: 10.3390/coatings13030590.

[19] I. S. Ovchinnikov, K. A. Vorotilov, D. S. Seregin, and G. Yu Dalskaya, "Detection of idden defects in low-k dielectrics by atomic force microscopy," in *Journal of Physics: Conference Series*, Institute of Physics Publishing, Oct. 2019. doi: 10.1088/1742-6596/1327/1/012011.

[20] M. B. Lodi *et al.*, "Microwave Characterization and Modeling of the Carasau Bread Doughs during Leavening," *IEEE Access*, vol. 9, pp. 159833–159847, 2021, doi: 10.1109/ACCESS.2021.3131207.

[21] "IEEE Instrumentation & Measurement Magazine," 2007.

[22] H. Zhou *et al.*, "Multi-Band Sensing for Dielectric Property of Chemicals Using Metamaterial Integrated Microfluidic Sensor," *Sci Rep*, vol. 8, no. 1, Dec. 2018, doi: 10.1038/s41598-018-32827-y.

[23] A. Tamer *et al.*, "Metamaterial based sensor integrating transmission line for detection of branded and unbranded diesel fuel," *Chem Phys Lett*, vol. 742, Mar. 2020, doi: 10.1016/j.cplett.2020.137169.

[24] M. G. Mayani, F. J. Herraiz-Martinez, J. M. Domingo, and R. Giannetti, "Resonator-Based Microwave Metamaterial Sensors for Instrumentation: Survey, Classification, and Performance Comparison," *IEEE Trans Instrum Meas*, vol. 70, 2021, doi: 10.1109/TIM.2020.3040484.

[25] A. Dhouibi, S. N. Burokur, A. De Lustrac, and A. Priou, "Compact metamaterial-based substrate-integrated Luneburg lens antenna," *IEEE Antennas Wirel Propag Lett*, vol. 11, pp. 1504–1507, 2012, doi: 10.1109/LAWP.2012.2233191.

[26] E. L. Chuma and T. Rasmussen, “Metamaterial-Based Sensor Integrating Microwave Dielectric and Near-Infrared Spectroscopy Techniques for Substance Evaluation,” *IEEE Sens J*, vol. 22, no. 20, pp. 19308–19314, Oct. 2022, doi: 10.1109/JSEN.2022.3202708.

[27] A. Grbic, R. Merlin, E. M. Thomas, and M. F. Imani, “Near-field plates: Metamaterial surfaces/arrays for subwavelength focusing and probing,” *Proceedings of the IEEE*, vol. 99, no. 10. Institute of Electrical and Electronics Engineers Inc., pp. 1806–1815, 2011. doi: 10.1109/JPROC.2011.2106191.

[28] IEEE Staff and IEEE Staff, *2012 IEEE 62nd Electronic Components and Technology Conference.*

[29] A. Tamer *et al.*, “Transmission Line Integrated Metamaterial Based Liquid Sensor,” *J Electrochem Soc*, vol. 165, no. 7, pp. B251–B257, 2018, doi: 10.1149/2.0191807jes.

[30] A. Hossain *et al.*, “Microwave brain imaging system to detect brain tumor using metamaterial loaded stacked antenna array,” *Sci Rep*, vol. 12, no. 1, Dec. 2022, doi: 10.1038/s41598-022-20944-8.

[31] M. T. Islam, M. T. Islam, M. Samsuzzaman, H. Arshad, and H. Rmili, “Metamaterial Loaded Nine High Gain Vivaldi Antennas Array for Microwave Breast Imaging Application,” *IEEE Access*, 2020, doi: 10.1109/ACCESS.2020.3045458.

[32] L. Su, J. Mata-Contreras, P. Vélez, and F. Martín, “A Review of Sensing Strategies for Microwave Sensors Based on Metamaterial-Inspired Resonators: Dielectric Characterization, Displacement, and Angular Velocity Measurements for Health Diagnosis, Telecommunication, and Space Applications,” *International Journal of Antennas and Propagation*, vol. 2017. Hindawi Limited, 2017. doi: 10.1155/2017/5619728.

[33] S. Mukherjee, X. Shi, L. Udpa, S. Udpa, Y. Deng, and P. Chahal, “Design of a Split-Ring Resonator Sensor for Near-Field Microwave Imaging,” *IEEE Sens J*, vol. 18, no. 17, pp. 7066–7076, Sep. 2018, doi: 10.1109/JSEN.2018.2852657.

[34] M. A. Aldhaeebi, T. S. Almoneef, H. Attia, and O. M. Ramahi, “Near-field microwave loop array sensor for breast tumor detection,” *IEEE Sens J*, vol. 19, no. 24, pp. 11867–11872, Dec. 2019, doi: 10.1109/JSEN.2019.2936993.

[35] M. A. Abou-Khousa and A. Haryono, “Array of Planar Resonator Probes for Rapid Near-Field Microwave Imaging,” *IEEE Trans Instrum Meas*, vol. 69, no. 6, pp. 3838–3846, Jun. 2020, doi: 10.1109/TIM.2019.2937532.

[36] A. Grbic, R. Merlin, E. M. Thomas, and M. F. Imani, “Near-field plates: Metamaterial surfaces/arrays for subwavelength focusing and probing,” *Proceedings of the IEEE*, vol. 99, no. 10. Institute of Electrical and Electronics Engineers Inc., pp. 1806–1815, 2011. doi: 10.1109/JPROC.2011.2106191.

[37] IEEE Staff and IEEE Staff, *2011 IEEE/MTT-S International Microwave Symposium.*

[38] K. Guven and E. Ozbay, “Near field imaging in microwave regime using double layer split-ring resonator based metamaterial,” *Opto-Electronics Review*, vol. 14, no. 3, pp. 213–216, 2006, doi: 10.2478/s11772-006-0028-7.

[39] IEEE Staff and IEEE Staff, *2011 IEEE/MTT-S International Microwave Symposium.*

[40] A. Ahmed, V. Kumari, and G. Sheoran, “Non-Destructive Dielectric Measurement and Mapping Using Microwave holography,” in *2022 2nd Asian Conference on Innovation in Technology, ASIANCON 2022*, Institute of Electrical and Electronics Engineers Inc., 2022. doi: 10.1109/ASIANCON55314.2022.9909059.

[41] H. Lee, S. Arakelyan, B. Friedman, and K. Lee, “Temperature and microwave near field imaging by thermo-elastic optical indicator microscopy,” *Sci Rep*, vol. 6, Dec. 2016, doi: 10.1038/srep39696.

[42] H. Lee, Z. Baghdasaryan, B. Friedman, and K. Lee, “Detection of a Conductive Object Embedded in an Optically Opaque Dielectric Medium by the Thermo-Elastic Optical Indicator Microscopy,” *IEEE Access*, vol. 7, pp. 46084–46091, 2019, doi: 10.1109/ACCESS.2019.2908885.

[43] H. Lee, Z. Baghdasaryan, B. Friedman, and K. Lee, “Detection of a Conductive Object Embedded in an Optically Opaque Dielectric Medium by the Thermo-Elastic Optical Indicator Microscopy,” *IEEE Access*, vol. 7, pp. 46084–46091, 2019, doi: 10.1109/ACCESS.2019.2908885.

[44] Z. Baghdasaryan, A. Babajanyan, L. Odabashyan, J. H. Lee, B. Friedman, and K. Lee, “Visualization of microwave near-field distribution in sodium chloride and glucose aqueous solutions by a thermo-elastic optical indicator microscope,” *Sci Rep*, vol. 11, no. 1, Dec. 2021, doi: 10.1038/s41598-020-80328-8.

[45] S. Hamelo, J. Yang, and H. Lee, “Detection of Defects in a Dielectric Material by Thermo-Elastic Optical Indicator Microscopy,” *IEEE Access*, vol. 11, pp. 45961–45971, 2023, doi: 10.1109/ACCESS.2023.3274534.

[46] Z. Baghdasaryan, A. Babajanyan, L. Odabashyan, H. Lee, B. Friedman, and K. Lee, “Visualization of Microwave Heating formesh-Patterned Indium-tin-Oxide by a Thermo-Elastic Optical Indicator Microscope,” 2018.

[47] H. Lee, “Detection of Air Bubbles and Liquid Droplet in a Dielectric Tube by Thermo-Elastic Optical Indicator Microscopy,” *IEEE Access*, vol. 10, pp. 33537–33546, 2022, doi: 10.1109/ACCESS.2022.3162247.

[48] Y. I. Abdulkarim *et al.*, “A Review on Metamaterial Absorbers: Microwave to Optical,” *Frontiers in Physics*, vol. 10. Frontiers Media SA, Apr. 29, 2022. doi: 10.3389/fphy.2022.893791.

[49] Y. Zhang, J. Zhao, J. Cao, and B. Mao, “Microwave metamaterial absorber for non-destructive sensing applications of grain,” *Sensors (Switzerland)*, vol. 18, no. 6, Jun. 2018, doi: 10.3390/s18061912.

[50] H. Huang, H. Xia, W. Xie, Z. Guo, H. Li, and D. Xie, “Design of broadband graphene-metamaterial absorbers for permittivity sensing at mid-infrared regions,” *Sci Rep*, vol. 8, no. 1, Dec. 2018, doi: 10.1038/s41598-018-22536-x.

[51] M. Bakir, M. Karaaslan, O. Akgol, O. Altintas, E. Unal, and C. Sabah, “Sensory applications of resonator-based metamaterial absorber,” *Optik (Stuttg)*, vol. 168, pp. 741–746, Sep. 2018, doi: 10.1016/j.ijleo.2018.05.002.

CHAPTER 7

Conclusions

This work investigated the effect of thin film thickness on the optical indicator (OI) and the integration of metamaterial absorbers (MM-ABS) with the OI to further improve the measurement sensitivity of TEOIM through the microwave absorption enhancement within the OI. Additionally, it significantly contributed to the advancement of TEOIM for non-destructive microwave measurements by developing a novel approach the dielectric measurement and mapping.

The study demonstrated a direct correlation between the thickness of aluminum thin films and the sensitivity of microwave H-MWNF measurements. As the film thickness decreased, the sensitivity of the optical indicator increased. Specifically, the OI with a thickness of 10nm exhibited higher sensitivity compared to optical indicators with film thicknesses of 25nm, 50nm, 75nm, and 100nm at an input microwave power of 30 dBm.

The integration of MM-ABS with the OI showed an improvement in microwave absorption capacity and measurement sensitivity, particularly at the resonance frequency of 11.5 GHz. At this frequency, the sensitivity of TEOIM achieved a 10-time improvement compared to the configuration without MM-ABS. The enhanced sensitivity performance was rigorously tested, revealing increased detection capabilities in field measurements. The integration of MM-ABS also shows the potential of TEOIM for non-destructive dielectric measurements and mapping, opening new possibilities for applications in diverse fields, including material characterization, quality control, biomedical research, and defect identification.

Looking to the future, there are possibilities for further research. Fine-tuning the thickness of aluminum thin film and additives in the deposition process is a promising way to achieve

even higher sensitivity in microwave magnetic field measurements. Investigating different metamaterial absorber geometries and configurations can provide the opportunity to improve the results. In particular, the spatial resolution of dielectric mapping depends on the size of the resonator on the MM-ABS and the spacing between the resonators. Smaller resonator dimensions in combination with a smaller spacing promise a higher spatial resolution and extend the possibilities of this innovative method.